



# 1 Unusual *Hemiaulus* Bloom Influences Ocean Productivity in 2 Northeast U.S. Shelf Waters

3 S. Alejandra Castillo Cieza<sup>1</sup>, Rachel H.R. Stanley<sup>1\*</sup>, Pierre Marrec<sup>2</sup>, Diana N. Fontaine<sup>2</sup>, E.  
4 Taylor Crockford<sup>3</sup>, Dennis J. McGillicuddy Jr. <sup>3</sup>, Arshia Mehta<sup>1</sup>, Susanne Menden-Deuer<sup>2</sup>, Emily  
5 E. Peacock<sup>3</sup>, Tatiana A. Rynearson<sup>2</sup>, Zoe O. Sandwith<sup>3,4</sup>, Weifeng (Gordon) Zhang<sup>3</sup>, and Heidi  
6 M. Sosik<sup>3</sup>

7 <sup>1</sup>Chemistry Department, Wellesley College, Wellesley, 02481, USA

8 <sup>2</sup>Graduate School of Oceanography, University of Rhode Island, Narragansett, 02882, USA

9 <sup>3</sup>Woods Hole Oceanographic Institution, Woods Hole, MA, 02543, USA

10 <sup>4</sup>Now at the Hakai Institute, Pruth Harbour, Calvert Island, BC, Canada

11 \*Correspondence to: Rachel H. R. Stanley (rachel.stanley@wellesley.edu)

12 **Abstract.** Ocean production and trophic transfer rates, including Net Community Production (NCP), Net Primary  
13 Production (NPP), Gross Oxygen Production (GOP), and microzooplankton grazing rates are key metrics for  
14 understanding marine ecosystem dynamics and impacts on biogeochemical cycles. Because of its temperate location  
15 and high dynamic range of environmental conditions and long-term human utilization, the long-term ecological  
16 research site in the coastal Northeastern U.S. Shelf (NES) of the Northwestern Atlantic Ocean offers an ideal  
17 opportunity to understand how productivity shifts in response to changes in planktonic community composition.  
18 While small phytoplankton usually dominate in the NES waters during the summer, a bloom of the large diatom  
19 genus *Hemiaulus*, with N<sub>2</sub> fixing symbionts, was observed in the mid-shelf region during the summer of 2019. NCP  
20 was 2.5 to 9 times higher when *Hemiaulus* dominated compared to NCP throughout the same geographic area  
21 during the summers of 2020–2022. The *Hemiaulus* bloom in summer 2019 also coincided with higher trophic  
22 transfer efficiency from phytoplankton to microzooplankton, higher GOP and NPP, and higher sea surface  
23 temperatures than summers 2020-2022. This study shows that the presence of an atypical phytoplankton community  
24 that alters the typical size distribution of the primary producers can greatly influence productivity and trophic  
25 transfer, highlighting the dynamic nature of the coastal ocean. Notably, summer 2018 NCP levels were also high  
26 although no atypical phytoplankton community was present. A better understanding of the dynamics of the NES in  
27 terms of biological productivity is of primary importance, especially in the context of changing environmental  
28 conditions due to climate processes.

## 29 1 Introduction

30 Oceans regulate atmospheric carbon dioxide (CO<sub>2</sub>) concentrations and support life on Earth via several mechanisms  
31 (Friedlingstein et al., 2022). One of these mechanisms is the biological pump, which involves biological, physical,  
32 and chemical processes that aid in transporting and sequestering organic carbon from CO<sub>2</sub> (Boyd et al., 2019). As  
33 the main primary producers in the ocean, phytoplankton play a major role in the biological pump (Field et al., 1998).  
34 Diatoms, a type of photosynthetic algae, are believed to account for nearly half of net marine primary productivity  
35 globally and are important contributors to the biological pump (Jin et al., 2006). Diatoms characteristically thrive in  
36 nutrient-rich surface layers and turbulent conditions, and are thus typically found at high latitudes and in coastal  
37 upwelling regions (Armbrust, 2009). However, new technology (e.g., molecular biology and imaging) has revealed  
38 that diatoms may be more prevalent in low nutrient, oligotrophic systems than traditionally considered (Malviya et  
39 al., 2016), likely due to unique metabolic capabilities involving nutrient acquisition strategies that enable their  
40 survival in low nutrient regimes.

41 One specific metabolic capability within diatoms is the ability to form a symbiosis with nitrogen-fixing  
42 cyanobacteria. This symbiosis, known as a diatom-diazotroph association has been observed around the globe,  
43 mostly in oligotrophic regions (Foster and Zehr, 2019), but also in temperate continental shelf waters (Wang et al.,  
44 2021). Furthermore, some diatom-diazotroph association have the capability to grow very quickly, forming  
45 localized blooms (Villareal et al., 2011). Diatom-diazotroph blooms, specifically involving the diatom genus



46 *Hemiaulus* and the symbiont *Richelia*, have been found in warm, stratified waters in various regions around the  
47 globe and have been associated with high carbon export observed via a combination of modern oceanographic  
48 measurements and paleo-flux case studies (Kemp and Villareal, 2013, Malviya et al., 2016). Examples include  
49 blooms in the eastern Equatorial Atlantic (Foster and Zehr, 2006), tropical North Atlantic (Carpenter et al., 1999,  
50 Subramaniam et al., 2008), North Pacific Subtropical Gyre (Dore et al., 2008, Villareal et al., 2011), and South  
51 China Sea (Grosse et al., 2010). Furthermore, at the ALOHA site in the Pacific Ocean north of Hawaii, blooms of  
52 the *Hemiaulus-Richelia* association can last as long as 30 days and contribute significantly (20%) to annual carbon  
53 flux in this region (Karl et al., 2012, Kemp and Villareal, 2018). As described by these examples, diatoms with  
54 nitrogen-fixing symbionts are thus important contributors to primary productivity and carbon export, especially at  
55 times when surface waters are depleted of dissolved inorganic nitrogen (Pyle et al., 2020, Tang et al., 2020).

56 An intense bloom of *Hemiaulus* and its symbiont *Richelia* was observed in summer 2019 in temperate  
57 Northeast U.S. Shelf (NES) surface waters. The NES region in the Northwestern Atlantic Ocean is particularly  
58 productive, favoring enhanced inorganic carbon sequestration by the biological pump, and supports an ecologically  
59 and economically important ecosystem (Townsend et al., 2006). Like other marine regions, the NES ecosystem is  
60 fueled by phytoplankton which are the main primary producers and fundamental components to ecosystem function  
61 (e.g. Mouw and Yoder, 2005, O'Reilly and Zetlin, 1998, Yoder et al., 2002). Productivity is heavily influenced by  
62 abiotic factors in the NES region. For instance, strong seasonal variations in water temperature, stratification and  
63 cross-shelf advection on the NES affect nutrient supply and lead to seasonal shifts in phytoplankton productivity and  
64 species composition (Li et al., 2015, Oliver et al., 2022, Zhang et al., 2023). Furthermore, the water temperature of  
65 the NES is rising faster than the global average (Chen et al., 2020, Karmalkar and Horton, 2021, Shearman and  
66 Lentz, 2010), leading to unknown consequences for phytoplankton community composition and productivity within  
67 this important and dynamic coastal region.

68 To further understand phytoplankton population dynamics and their influence on the ocean's biological  
69 pump, the NES Long-Term Ecological Research (NES-LTER, <https://nes-lter.whoi.edu/>) project investigates  
70 primary productivity, food web structure and ecosystem dynamics with a focus on southern New England coastal  
71 waters. As part of the NES-LTER project, phytoplankton and zooplankton community composition, phytoplankton  
72 growth rates, microzooplankton grazing rates, and productivity rates are determined on week-long research cruises  
73 which have occurred quarter-annually since 2018. To quantify productivity, several different rates are estimated  
74 from data collected on these cruises, including Gross Oxygen Production (GOP), Net Primary Production (NPP),  
75 Net Community Production (NCP) and export efficiency ratios (NCP/GOP). GOP is similar to Gross Primary  
76 Production; it represents total photosynthesis in oxygen units and also includes photoprocesses that produce oxygen  
77 (Juraneck and Quay, 2013). NPP is photosynthetic production minus autotrophic respiration and thus represents the  
78 net production activity of the phytoplankton community. NCP is the balance of photosynthesis and community  
79 respiration (autotrophic plus heterotrophic) and is equal, on long enough spatial and temporal scales, to the amount  
80 of carbon exported out of the surface of the ocean (Emerson, 2014). The NCP/GOP ratio, analogous to the f-ratio  
81 (Dugdale and Goering, 1967), is indicative of export efficiency, with a high ratio implying that the community is  
82 exporting most of the carbon (organic matter) produced and recycling only a little (Juraneck and Quay, 2013).

83 The composition and size structure of the phytoplankton community in the NES-LTER study are  
84 investigated concurrently from automated imaging and size-fractionated chlorophyll-a (Chl-a). In winter, the NES  
85 waters tend to be nutrient-rich due to enhanced vertical mixing and input of river and estuary waters that promote  
86 high levels of surface Chl-a, with a dominance of large phytoplankton cells (>10  $\mu\text{m}$ ) that are growing slowly  
87 (Marrec et al., 2021). Conversely, during a typical summer, nutrients become depleted in the surface mixed layer,  
88 leading to low Chl-a concentrations dominated by fast-growing small phytoplankton cells (<10  $\mu\text{m}$ ) (Marrec et al.,  
89 2021, O'Reilly and Zetlin, 1998).

90 To complement production estimates and phytoplankton community structure observations, the flow of  
91 carbon from primary producers to higher trophic levels is investigated. Microzooplankton, protists smaller than 200  
92  $\mu\text{m}$ , are a crucial link between primary producers and higher trophic levels because they often consume 60–70% of  
93 daily primary production (Landry and Calbet, 2004, Schmoker et al., 2013). In the NES, while phytoplankton grow  
94 faster during the summer than in winter, microzooplankton grazing rates tend to stay relatively constant across  
95 seasons (Marrec et al., 2021). Thus, during winter, phytoplankton growth rates and microzooplankton grazing rates  
96 are typically well coupled and show a close 1:1 ratio, with microzooplankton consuming most of the primary  
97 production (Marrec et al., 2021). During the summer, the phytoplankton growth and microzooplankton grazing rates  
98 are typically decoupled, with higher growth rates than in winter, but grazing rates in the same range, leading to less  
99 than 50% of the primary production consumed by microzooplankton. The degree of coupling between  
100 microzooplankton grazing and phytoplankton growth rates is associated with phytoplankton size structure (Marrec et



101 al., 2021) and likely composition, and is an important indicator of the trophic transfer efficiency from phytoplankton  
102 to microzooplankton, at the basis of the planktonic food web.

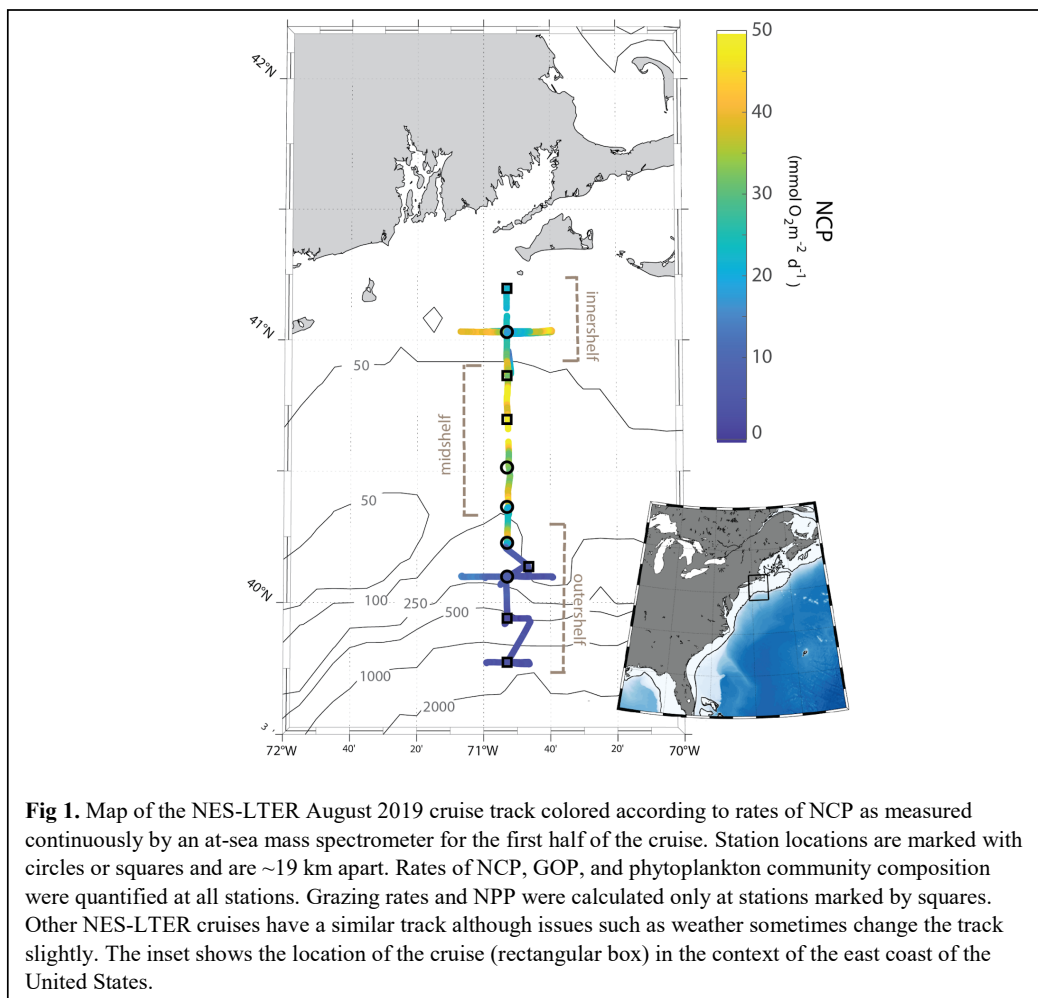
103 Here, we examined the association between productivity, phytoplankton composition and  
104 microzooplankton grazing, key components of trophic transfer efficiency and thus ecosystem function. During a  
105 NES-LTER cruise in summer 2019, we observed an anomalous relationship between growth and grazing rates, as  
106 well as dramatically different productivity rates and community composition compared to other summer cruises in  
107 the NES region. We thus investigated how a diatom bloom of *Hemiaulus* with diazotrophic symbionts affected  
108 metrics of productivity and grazing on the NES during the summer of 2019. Our results provide insights into the  
109 effects of community composition on productivity rates.

## 110 2 Methods

111 Measurements of environmental conditions, chemical and biological stocks, and productivity and grazing rates were  
112 conducted on multiple cruises within the framework of the NES-LTER program (Table 1). Measurements from three  
113 other cruises from different projects on the NES were also included in this analysis for comparison (project names in  
114 Table 1). From this time series, we were able to better understand an event observed on the 2019 NES-LTER  
115 summer cruise (EN644) which occurred from August 19 to 25 (Table 1). Some data during that event, such as  
116 surface seawater temperature (SST), salinity (SSS), NCP rates, and phytoplankton composition were collected  
117 continuously from the underway system (i.e., km-scale resolution), while other parameters (e.g., NPP, grazing rates,  
118 Chl-a, nutrients) were measured discretely at the NES-LTER stations. Main stations were located with ~ 19 km  
119 spacing on a north-to-south transect primarily along 70° 53' W (Fig. 1). In particular, the mid-shelf region, which is  
120 where the *Hemiaulus* bloom primarily occurred, corresponds to 50 – 100 m water depth (Fig. 1) and contains 4  
121 stations. At each station, water was collected via Niskin bottles mounted on a CTD-rosette (conductivity-  
122 temperature-depth, Seabird SBE32 Carousel Water Sampler). The CTD-rosette system consisted of a 24-bottle  
123 rosette frame with 10-L Niskin bottles. Depth, temperature, and salinity were collected with a SBE911 CTD  
124 (Seabird Electronics) equipped with additional sensors for chlorophyll fluorescence (WET Labs ECO-AFL/FL),  
125 photosynthetically active radiation (PAR, Biospherical Instruments® QSP2000), and beam attenuation (WET Labs  
126 C-Star 25-cm transmissometer). The Niskin bottles were closed at various depths ranging from surface to near  
127 bottom, based on the depths of the mixed layer, euphotic zone, and Chl-a maximum. Water from the Niskins was  
128 used to quantify a number of parameters as described in Sections 2.2 through 2.5.  
129 ).

130 **Table 1.** Dates of the summer cruises, as well as project and ship names and cruise numbers, that are presented in  
131 this paper. Project name abbreviations are as follows: OTZ– Ocean Twilight Zone, SPIROPA–Shelfbreak  
132 Productivity Interdisciplinary Research Operation at the Pioneer Array (Oliver et al., 2021), and EcoMon–  
133 Ecosystem Monitoring program run by the National Oceanic and Atmospheric Administration.

Cruise Name	Start date/End date	Project name	Ship name
EN617	20 July 2018 – 25 July 2018	NES-LTER	<i>R/V Endeavor</i>
TN368	05 July 2019 – 18 July 2019	SPIROPA	<i>R/V Thomas G. Thompson</i>
HB1907	25 July 2019 – 08 Aug 2019	OTZ	<i>NOAA Ship Henry B Bigelow</i>
GU1902	16 Aug 2019 – 29 Aug 2019	EcoMon	<i>NOAA Ship Gordon Gunter</i>
EN644	20 Aug 2019 – 25 Aug 2019	NES-LTER	<i>R/V Endeavor</i>
EN655	25 July 2020 – 28 July 2020	NES-LTER	<i>R/V Endeavor</i>
EN668	16 July 2021 – 21 July 2021	NES-LTER	<i>R/V Endeavor</i>
EN687	29 July 2022 – 03 Aug 2022	NES-LTER	<i>R/V Endeavor</i>



134 The underway system consisted of continuous surface seawater pumped throughout the ship by an impeller pump  
135 and a diaphragm pump located near the ship's bow. Using water from the impeller pump, continuous measurements  
136 of surface temperature and salinity were obtained from a Seabird SBE38 (temperature) sensor installed at the water  
137 intake and by a Seabird SBE45 sensor (temperature and salinity) located further away in the underway system.  
138 Because the diaphragm pump is less likely to damage plankton, its underway flow was used for measurements to  
139 quantify NCP (Section 2.1), GOP (Section 2.2) and phytoplankton community composition (Section 2.6

## 140 2.1 Net Community Production

141 Net community production rates were calculated from  $O_2/Ar$  ratios measured by an at-sea Equilibrator Inlet Mass  
142 Spectrometer (EIMS) (Cassar et al., 2009) analyzing water from the ship's underway system and from discrete  
143 samples collected from both CTD Niskin bottles and from the underway system. The EIMS was used to collect  
144 continuous data on  $O_2/Ar$  ratios via the diaphragm pump of the underway system that, on the *R/V Endeavor*, pumps  
145 seawater from a depth of 5 m. The underway system seawater flows through a debubbler into a bucket at a constant  
146 rate that allows for continuous overflow for consistent head pressure. Water is then pumped from the bucket at ~1.1  
147  $L\ min^{-1}$  by a gear pump through two filters: a bag with a 25- $\mu m$  pore size, and a 2-layered sock with a 5- $\mu m$  inner  
148 and 100- $\mu m$  outer pore size. The gear pump then pushes the water through an equilibrator membrane contactor



149 cartridge (Liqui-Cel Extra-Flow 2.5x8 model G540). The equilibrated headspace gas from the cartridge is then dried  
 150 by flowing through the dessicants Nafion and Drierite and then passed via a fused silica capillary into a Hiden  
 151 Residual Gas Analyzer (RGA) (HAL 7) quadrupole mass spectrometer. Details of the equilibration method can be  
 152 found in (2016), but in this instance were modified to not use SAES getters as they would have removed the O<sub>2</sub>. The  
 153 EIMS was operated throughout the whole cruise (starting one hour after the ship left port and ending a few hours  
 154 before return to port). To calibrate the mass spectrometer, the capillary was switched to an air inlet for twenty  
 155 minutes approximately every six hours as the ratio of O<sub>2</sub>/Ar in air is stable and well-known. Additionally, bottle  
 156 samples were collected from the underway system at least once per day and were subsequently measured on an  
 157 isotope ratio mass spectrometer at Woods Hole Oceanographic Institution (see Section 2.2). These bottle samples  
 158 were used to provide additional calibration as necessary—such additional corrections changed the O<sub>2</sub>/Ar ratios by at  
 159 most 0.67%.

160 The O<sub>2</sub>/Ar ratios were then used to calculate NCP (Hendricks et al., 2004, Juranek and Quay, 2005, Stanley  
 161 et al., 2010). With data from the EIMS and the bottle samples, the biological oxygen saturation Δ(O<sub>2</sub>/Ar) was  
 162 calculated via the equation below:

$$163 \quad \Delta \left( \frac{O_2}{Ar} \right) = \frac{\left( \frac{O_2}{Ar} \right)_{\text{smp}}}{\left( \frac{O_2}{Ar} \right)_{\text{eq}}} - 1 \quad (1)$$

164 where (O<sub>2</sub>/Ar)<sub>smp</sub> represents the ratio of O<sub>2</sub> to Ar ion currents detected by the EIMS after being calibrated with  
 165 bottle data, and (O<sub>2</sub>/Ar)<sub>eq</sub> represents the ratio of equilibrium concentrations of the gases determined from the gases'  
 166 solubility (Garcia and Gordon, 1992, Hamme and Emerson, 2004) at the seawater temperature and salinity.

167 The NCP integrated over the mixed layer, in units of mmol O<sub>2</sub> m<sup>-2</sup> d<sup>-1</sup>, is calculated as

$$168 \quad NCP = \Delta \left( \frac{O_2}{Ar} \right) [O_2]_{\text{eq}} k \rho \quad (2)$$

169 where [O<sub>2</sub>]<sub>eq</sub> represents the equilibrium concentration of O<sub>2</sub> at the relevant temperature and salinity (mmol kg<sup>-1</sup>), *k* is  
 170 the weighted gas transfer velocity (m d<sup>-1</sup>), and *ρ* is the density of seawater (kg m<sup>-3</sup>) (Millero and Poisson, 1981). The  
 171 weighted gas transfer velocity is a time-weighted average from over the past 30 days calculated as described in  
 172 Reuer et al. (2007), with the gas exchange parameterization of Stanley et al., (2009) and wind speeds from NCEP  
 173 Reanalysis (Kalnay et al., 1996, Kistler et al., 2001). Many physical considerations altering O<sub>2</sub> saturations, such as  
 174 changes in temperature and bubble injection, do not need to be considered due to the inclusion of Ar which has  
 175 similar solubility and diffusivity as O<sub>2</sub>; however, a few assumptions were made for these calculations. Firstly, this  
 176 equation assumes steady state within the mixed layer, i.e. no change in O<sub>2</sub>/Ar in the ocean with time. While O<sub>2</sub>/Ar  
 177 was likely changing in actuality, assuming steady state simply means that the rates calculated reflect an  
 178 exponentially weighted average of NCP over the past few residence times of oxygen (residence time equals a few  
 179 days in these conditions) (Teeter et al., 2018). Thus, the assumption of steady state does not majorly impact our  
 180 conclusions. We were not able to calculate the time rate of change term in O<sub>2</sub>/Ar (Manning et al., 2017b) because  
 181 the cruise was not Lagrangian, and even though the ship returned to the same geographic location, the water at that  
 182 location changed due to ocean currents. To check the assumption that there is negligible respiration within the ship's  
 183 lines (Juranek et al., 2010), bottle samples were collected in duplicate from Niskins at the same time as samples  
 184 were collected from the underway system several times during every cruise; gas concentrations in the bottle samples  
 185 from the underway and Niskin were identical within measurement errors, confirming there was no detectable  
 186 respiration in the ship's line.

## 187 2.2 Gross Oxygen Production

188 Discrete samples of triple oxygen isotopes (TOI) were collected from the surface Niskin bottles on the CTD-rosette  
 189 system at all stations as well as from the underway system between stations. Samples from the CTD-rosette system  
 190 were also collected from bottles fired at ~ 5 m below the mixed layer and often one greater depth to provide  
 191 information for assessing whether vertical corrections to O<sub>2</sub>/Ar ratios were significant. Samples were collected in  
 192 custom-made ~500-mL sample bottles which were pre-poisoned with 100 μl of saturated mercuric chloride solution  
 193 and filled with around 300 mL of seawater from the underway system or from the Niskin at each station (Stanley et  
 194 al., 2015). Samples were brought to Woods Hole Oceanographic Institution where they were analyzed for TOI with  
 195 a custom-made processing line and a ThermoFisher MAT 253 isotope ratio mass spectrometer as detailed in Stanley  
 196 et al (2015). The same samples were also analyzed for O<sub>2</sub>/Ar which yielded rates of NCP from discrete data as well  
 197 as an independent method for calibrating the EIMS (see above). Corrections for the effect of argon on the triple  
 198 oxygen isotope ratio and the effect of varying sizes of the sample vs. reference standard were made for every



199 sample. Reproducibility from duplicate samples collected on these cruises ranged from 4 to 8 per meg for  $^{17}\Delta$ , 0.008  
 200 to 0.03 per mil for  $\delta^{17}\text{O}$ , and 0.008 to 0.05 per mil for  $\delta^{18}\text{O}$  depending on the cruise.

201 From these samples, GOP is calculated in units of  $\text{mmol O}_2 \text{ m}^{-2} \text{ d}^{-1}$  following Prokopenko et al., (2011)  
 202 according to:

$$203 \quad \text{GOP} = k \text{O}_{\text{eq}} \frac{\frac{X_{\text{dis}}^{17} - X_{\text{eq}}^{17}}{X_{\text{dis}}^{17}} - \lambda \frac{X_{\text{dis}}^{18} - X_{\text{eq}}^{18}}{X_{\text{dis}}^{18}}}{\frac{X_{\text{p}}^{17} - X_{\text{eq}}^{17}}{X_{\text{dis}}^{17}} - \lambda \frac{X_{\text{p}}^{18} - X_{\text{eq}}^{18}}{X_{\text{dis}}^{18}}} \quad (3)$$

204 where  $k$  again represents the time-weighted gas transfer velocity ( $\text{m d}^{-1}$ ),  $\text{O}_{\text{eq}}$  represents the equilibrium  
 205 concentration of oxygen,  $\lambda$  represents the respiration slope factor = 0.5179,  $X_{\text{dis}}^*$  represents the ratio of isotopes  
 206 ( $^*\text{O}/^{16}\text{O}$ ) dissolved in the sample,  $X_{\text{eq}}^*$  represents the ratio of isotopes ( $^*\text{O}/^{16}\text{O}$ ) dissolved in seawater equilibrated  
 207 with the atmosphere, and  $X_{\text{p}}^*$  stands for the ratio of isotopes ( $^*\text{O}/^{16}\text{O}$ ) in oxygen that was produced via  
 208 photosynthesis. The photosynthetic end member used was the average of the phytoplankton value determined by  
 209 Barkan and Luz (2011), and Vienna Standard Mean Ocean Water (VSMOW) was used for the isotopic composition  
 210 of oxygen in  $\text{H}_2\text{O}$ . The actual isotopic composition of  $\text{H}_2\text{O}$  was measured in a subset of samples to see if corrections  
 211 needed to be made (Manning et al., 2017a). It was found to be very similar to VSMOW, leading to an error of less  
 212 than 10% in GOP due to isotopic water variations.

213 Confirmation that the water from the underway system was representative of the oceanic TOI signature of  
 214 dissolved oxygen was obtained by comparing samples collected from the underway system to those collected  
 215 concurrently from the surface Niskin bottle. All cruises, other than 2019, showed that there was statistically no  
 216 difference in TOI between water from the underway system and the CTD and thus that the water from the underway  
 217 system was representative of the mixed layer at that location and time. During the summer of 2019, the water from  
 218 the underway system had TOI values 4.1 per meg lower than that from the CTD – this is within measurement errors  
 219 but since it might have led to systematic biases, we corrected for this offset before calculating GOP from the data.  
 220 The GOP rates, along with the NCP rates, represent productivity integrated throughout the mixed layer.

### 221 2.3 Net Primary Productivity

222 Water samples for NPP were collected at 4-7 stations (cruise dependent) from 3-4 depths (station  
 223 dependent) from the Niskins on the CTD-rosette system. During collection, water was pre-filtered through 200- $\mu\text{m}$   
 224 mesh (to remove mesozooplankton) into acid-washed 2-L polycarbonate bottles. Water collection and associated  
 225 incubation occurred in triplicate for surface samples at each station. Bottles were spiked with a solution of 99%  
 226  $\text{NaH}^{13}\text{CO}_3$  (Cambridge Isotope Lab, Tewksbury, MA) for a final 10% enrichment of the dissolved inorganic carbon  
 227 (DIC) pool and placed in various mesh bags to simulate *in situ* light levels. Bottles were incubated for 24 h in clear  
 228 deck-board incubators with flowthrough seawater and Onset HOBO data loggers monitored tank water temperature.  
 229 At each station, the natural  $^{13}\text{C}$  in the water was determined from an un-spiked sample and dark carbon assimilation  
 230 was determined from a spiked dark bottle sample. Dark carbon assimilation was negligible (<1%) so no correction  
 231 for dark carbon assimilation was applied to this dataset.

232 The corresponding light levels at collection depths were determined using either PAR or beam attenuation  
 233 from the CTD cast for each station. When PAR data were not available (e.g., night-time casts), a relationship was  
 234 established (eq. 4) with previous daytime cast information between beam attenuation ( $c$ , measured by  
 235 transmissometer,  $\text{m}^{-1}$ ) and the light extinction coefficient ( $K_d$ ,  $\text{m}^{-1}$ ) for each cruise. During night-time casts,  $K_d$  was  
 236 estimated from the average  $c$  in the upper 10 m during the cast with the slope ( $m$ ) and intercept ( $b$ ) from the  
 237 daytime plot, according to equation 4:

$$238 \quad K_d = (m * At) + b \quad (4)$$

239 The appropriate shading in incubations (%PAR) for each depth of sample collection ( $z$ ) was estimated as:

$$241 \quad \%PAR = 100e^{-K_d \times z} \quad (5)$$

242 At the end of each incubation, bottles were filtered under low vacuum (5-10 in. Hg) over pre-combusted  
 243 Whatman GF/F filters (450°C; 6h). Filters were stored at -20°C until further analysis on shore. NPP rates were  
 244 quantified by measuring the incorporation of isotopically heavy carbon into phytoplankton biomass. Prior to  
 245 measuring  $^{13}\text{C}$  in the samples, filters were acid fumigated with concentrated HCl in a desiccator overnight to remove  
 246 inorganic carbon. They were dried in an oven at 60°C for 24 h, individually wrapped in tin capsules and analyzed on  
 247 a Carlo Erba NC2500 elemental analyzer interfaced with a Thermo Delta V+ isotope ratio mass spectrometer. The  $\delta$



248  $^{13}\text{C}$  values were reported relative to the international standard Vienna PeeDee Belemnite (Coplen, 1995) and  
 249 converted to atom percent values.

250 NPP rates were calculated from atom percent values with the equation from Hama et al. (1983)

$$251 \quad NPP = \frac{POC \cdot (a_{is} - a_{ns})}{t \cdot (a_{ic} - a_{ns})} \quad (6)$$

252 where NPP is the net primary production rate ( $\mu\text{g} \cdot \text{L}^{-1} \cdot \text{day}^{-1}$ ), POC is the particulate organic carbon; ( $\mu\text{g} \cdot \text{L}^{-1}$ ),  $t$  is  
 253 the incubation time (h),  $a_{is}$  is the atom % of  $^{13}\text{C}$  in the incubated sample,  $a_{ns}$  is the atom % of  $^{13}\text{C}$  in the natural  
 254 sample (un-spiked sample described above) and  $a_{ic}$  is the atom % of  $^{13}\text{C}$  in the total DIC pool. POC measurements  
 255 were blank corrected with the mean value of triplicate combusted filter blanks. The DIC concentration was  
 256 determined from salinity (S) according to the following equation from Parsons et al. (1984):

$$257 \quad DIC = ((S * 0.067) - 0.05) * 0.96 \quad (7)$$

258 NPP rates were integrated to the depth of the mixed layer (Table S1) to align with NCP and GOP integrated rate  
 259 calculations. The mixed layer depths were calculated from the temperature and salinity data from the CTD with the  
 260 threshold method where the mixed layer was declared to be the depth where the density difference between the  
 261 surface density and the mixed layer was greater than  $\Delta\sigma_\theta = 0.125 \text{ kg m}^{-3}$  (de Boyer Montegut et al., 2004). Mixed  
 262 layer depths were confirmed to be similar when a gradient criterion with a difference of  $0.0125 \text{ kg m}^{-3}$  was used  
 263 instead (Kara et al., 2000). Primary production rates for 2018 were estimated from the growth/grazing rates. The  
 264 surface values of phytoplankton growth rates were converted from Chl-a to carbon ( $\text{mg C m}^{-3} \text{ d}^{-1}$ ) with a constant  
 265 ratio of 50 which was then multiplied by the mixed layer depth to get values in  $\text{mg C m}^{-2} \text{ d}^{-1}$ .

## 266 2.4 Autotrophic and Heterotrophic Respiration

267 Assuming a photosynthetic quotient (O:C ratio) of 1.4, respiration rates were calculated from the productivity values  
 268 (GOP, NPP, and NCP) and following the relationships below:

$$269 \quad NPP = GOP - R_A \quad (8)$$

$$270 \quad NCP = NPP - R_H \quad (9)$$

271 where  $R_A$  is autotrophic respiration and  $R_H$  is heterotrophic respiration.

272

## 273 2.5 Growth Rates and Grazing rates

274 Rates of phytoplankton growth and protistan grazing were quantified with a 2-point modification of the dilution  
 275 method (Chen, 2015, Landry et al., 2008, Morison et al., 2020) following methods in Marrec et al. (2021). Briefly,  
 276 surface samples were collected at 4 to 7 stations throughout the cruise. For each sample, whole seawater (WSW)  
 277 from the Niskin bottles was transferred into a 10-L polycarbonate carboy through a 200- $\mu\text{m}$  mesh filter to remove  
 278 mesozooplankton predators. Diluent was prepared by gravity filtration through a 0.2  $\mu\text{m}$  membrane filter capsule  
 279 (PALL<sup>®</sup>) from the Niskin to the carboys and mixed with WSW to obtain a 20% WSW dilution. A total of 6 bottles  
 280 per experiment were prepared: 2 bottles with nutrient amended 20% WSW, 2 bottles with nutrient-amended WSW,  
 281 and 2 bottles with unamended WSW to assess nutrient limitation. Incubations took place for 24 h in a clear, 1m<sup>3</sup>  
 282 deck-board incubator. Paired bottles were placed into mesh bags that simulated the effective light availability in the  
 283 surface mixed layer, which corresponded to 65% of sea surface irradiance. Phytoplankton growth and grazing  
 284 mortality rates were then estimated from changes in Chl-a over the 24 h incubation. For dilution experiments, Chl-a  
 285 concentrations were obtained from triplicate 150-mL subsamples filtered on GF/F filters, after a 12-h dark extraction  
 286 period at room temperature in 95% ethanol and measured on a calibrated Turner 10 AU fluorometer. The full  
 287 extraction method is detailed in Marrec et al. (2021).

## 288 2.6 Discrete Chlorophyll-a sample collection and processing

289 Samples for Chl-a analysis were collected into brown amber bottles from Niskins on the CTD Rosette system. A  
 290 known sample volume (250-500 mL) was filtered at low pressure (5-10 in. Hg) through either a GF/F filter or a 20  
 291  $\mu\text{m}$  polycarbonate Sterlitech filter. Filters were transferred to either tissue capsules (GF/F) or cryogenic vials (20  
 292  $\mu\text{m}$ ) and then flash frozen in liquid nitrogen until extraction. Later, filters were extracted in 5 mL of 90% acetone for  
 293 24 hours in a dark refrigerator, then tubes were vortexed and centrifuged (only GF/F filters), and the solution was



294 measured on a calibrated Turner Designs Handheld Aquaflor fluorometer, acidified with 2 drops of 10%  
295 hydrochloric acid and measured again. Chl-a concentrations for different size fractions were calculated by  
296 difference.

## 297 **2.7 Satellite and radar data**

298 To look at variability in SST and surface Chl-a, a proxy for phytoplankton biomass, throughout the summers over  
299 multiple years, on a wider spatial and temporal scale than the at-sea chlorophyll data permitted, SST and surface  
300 Chl-a concentrations from remote sensing sources were retrieved and analyzed. In particular, both snapshots and  
301 monthly averages of MODIS (Moderate Resolution Imaging Spectroradiometer) SST and chlorophyll data with a  
302 horizontal resolution of 1 km were used to examine the spatial coverage of the *Hemiaulus* bloom in summer 2019  
303 (when it dominated phytoplankton biomass) and compare the surface temperature and chlorophyll in the NES region  
304 in summers 2018-2022.

305 To examine possible origins of the bloom water, backward particle trajectory simulations were carried out  
306 with the OceanParcels Python package <https://oceanparcels.org/index.html> (Lange and van Sebille, 2017). High  
307 frequency (HF) radar-measured sea surface velocity data in the NES region in Jul-Aug 2019 with 6-km spatial  
308 resolution and hourly temporal resolution were used as the background flow. Particles were released at mid-shelf  
309 sites along the NES-LTER transect on Aug 21, 2019 and advected backward for 30 days until Jul 22, 2019.

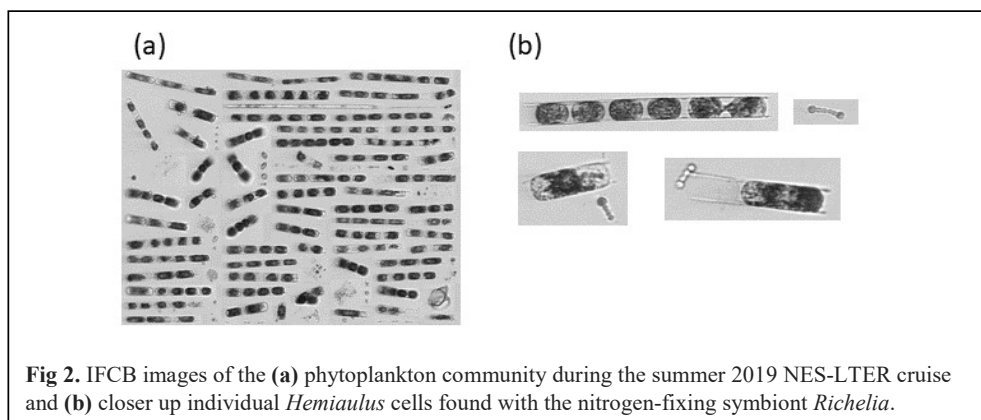
## 310 **2.8 Imaging FlowCytobot**

311 Composition of the phytoplankton community was assessed with Imaging FlowCytobots (IFCB; McLane Research  
312 Laboratories, Inc.). IFCB uses a combination of video and flow cytometry technology to capture images of plankton  
313 and other particles in the size range ~5-150  $\mu\text{m}$  (Olson and Sosik, 2007). During the cruises reported here, IFCB  
314 instruments were configured to record images of particles with laser-based chlorophyll fluorescence or light  
315 scattering signals above trigger thresholds and samples were pre-screened with 150  $\mu\text{m}$  Nitex. IFCB instruments  
316 were operated two ways. First, on all cruises, an IFCB was configured to sample 5 mL automatically from the ship's  
317 underway system every 25 minutes. Second, at stations occupied on the NES-LTER and SPIROPA cruises, IFCB  
318 instruments were used to analyze depth profiles from discrete samples collected with Niskin bottles. Typically, three  
319 5-mL subsamples were measured for each depth. The fraction of each 5-mL sample imaged by IFCB decreases with  
320 increasing trigger rate but is recorded precisely during sample acquisition enabling calculation of concentrations.  
321 IFCB image data were automatically analyzed following approaches developed for the IFCB time series at the  
322 Martha's Vineyard Coastal Observatory (MVCO) (Brownlee et al., 2016). In particular, cell biovolume was  
323 estimated from IFCB images (Moberg and Sosik, 2012) and converted to cell carbon following the relationships  
324 described by Menden-Deuer and Lessard (2000). IFCB images were classified with a convolutional neural network  
325 (CNN) trained to separate 155 categories of plankton and other particles observed at MVCO and across the NES  
326 region. We used the Inception v3 (Szegedy et al., 2016) CNN architecture as implemented in PyTorch, pre-trained  
327 with ImageNet (Russakovsky et al., 2015) and fine-tuned with an NES IFCB training set (97026 images, 155  
328 classes, 80-20 split for training and validation). In addition, an independent test set of manually annotated images in  
329 51 IFCB samples from EcoMon cruises was used to evaluate *Hemiaulus* quantification as a function of classifier  
330 score threshold. From this independent analysis, classifier predictions with scores above 0.9 performed very well for  
331 *Hemiaulus* (class-specific F1-score = 0.936; CNN-count vs. manual-count:  $r^2 = 0.999$ , slope = 0.915; intercept =  
332 0.005).

## 333 **2.9 Nutrients**

334 Dissolved inorganic nutrient concentrations (ammonium, phosphate, silicate, and nitrate + nitrite) were obtained  
335 from CTD bottle samples with duplicates. Seawater was passed through an EMD Millipore sterile Sterivex 0.22  $\mu\text{m}$   
336 filter with filtrate collected into acid-washed 20-ml scintillation vials (after triplicate rinses), which were then stored  
337 at -20 °C until analysis. Samples were processed at Woods Hole Oceanographic Institution's Nutrient Analytical  
338 Facility with a four-channel segmented flow SEAL AA3 HR Autoanalyzer. Detection levels are as follows: 0.01  
339  $\mu\text{mol L}^{-1}$  for silicate, 0.03  $\mu\text{mol L}^{-1}$  for phosphate, 0.04  $\mu\text{mol L}^{-1}$  for nitrate + nitrite, and 0.03  $\mu\text{mol L}^{-1}$  for  
340 ammonium.



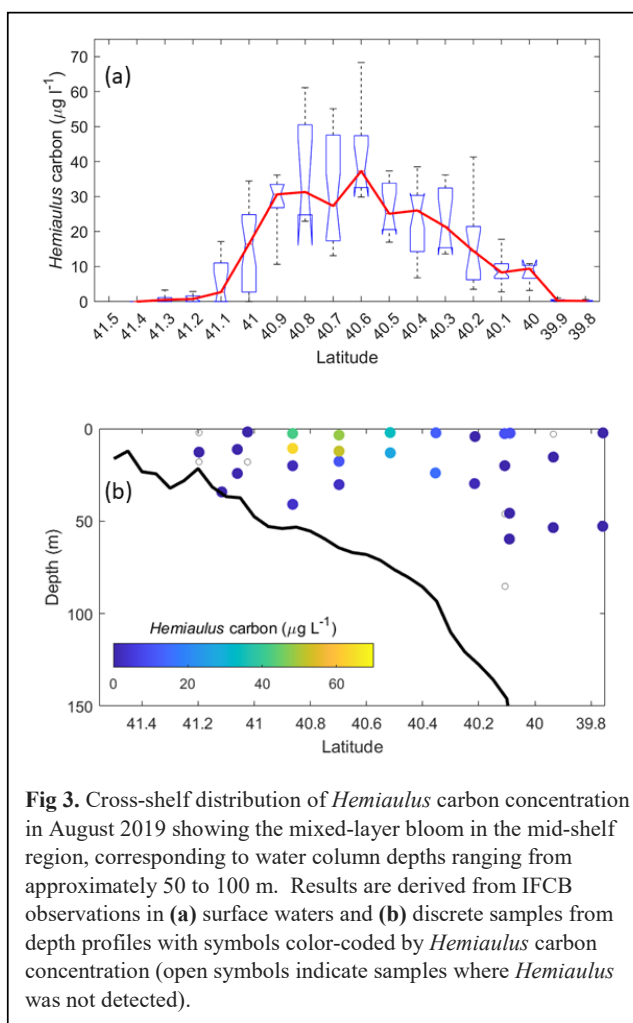


343 **Results**

344 **3.1 Hemiaulus distribution and**  
345 **Chlorophyll**

346 During the NES-LTER summer 2019 cruise,  
347 through automated image classification and  
348 analysis and through visual microscopic  
349 confirmation, a bloom of the diatom genus  
350 *Hemiaulus* was observed in the surface  
351 waters of the mid-shelf region (Fig. 2a).  
352 These images also showed N<sub>2</sub> fixing  
353 symbionts, namely *Richelia*, inside or next to  
354 the *Hemiaulus* cells (Fig. 2b). Additionally,  
355 *Hemiaulus* carbon was highest in the mid-  
356 shelf waters between latitudes of 40.1° N and  
357 41.1° N, a span of 111 km (Fig. 3a), with  
358 concentrations ranging from 6.8 to 68.3 μg L<sup>-1</sup>.  
359 This bloom was only observed in the  
360 surface waters of the mid-shelf region, as can  
361 be seen by discrete IFCB measurements from  
362 Niskin samples (Fig. 3b). *Hemiaulus* carbon  
363 concentrations observed in other years on  
364 NES-LTER transect cruises never reached  
365 values above 0.30 μg L<sup>-1</sup>.

366 The presence of the diatom bloom  
367 was consistent with the size-fractionated Chl-  
368 a data. Surface Chl-a concentrations in the  
369 mid-shelf region in summer are typically low  
370 (< 0.50 μg L<sup>-1</sup>, Fig. 4a) and progressively  
371 decrease with decreasing latitude. However,  
372 during the NES-LTER summer 2019, Chl-a  
373 concentrations were observed up to 3.50 μg  
374 L<sup>-1</sup> in the surface waters of the mid-shelf  
375 (mean Chl-a of 1.96 μg L<sup>-1</sup>, Table 2) with up  
376 to 80% of the Chl-a associated with the > 20  
377 μm fraction (Fig. 4c). This is in contrast to  
378 other summers when most of the Chl-a was





379 associated with the  $< 20 \mu\text{m}$   
380 fraction (Fig. 4b, d-f).  
381 Concentrations of Chl-a in the  $>$   
382  $20 \mu\text{m}$  size fraction and  
383 concentrations of *Hemiaulus*  
384 carbon in the NES-LTER  
385 summer 2019 cruise were larger  
386 at co-located sampling locations  
387 in the beginning of the cruise  
388 than at the end, suggesting that  
389 the bloom may have peaked  
390 before the cruise started and thus  
391 was in decline during the cruise  
392 period.

393 Monthly mean surface  
394 Chl-a concentrations from  
395 remote sensing were used to  
396 investigate if the observed  
397 differences in Chl-a and  
398 productivity between the  
399 summers were related to  
400 differences in the timing of the  
401 cruise as opposed to differences  
402 in community composition  
403 (Fig. S1). In many of the  
404 summers (2018, 2021, and  
405 2022), Chl-a in July was actually  
406 higher than in August, suggesting  
407 that the timing of the 2019 cruise  
408 (end of August instead of end of  
409 July) was not a factor in explaining  
410 the anomalous results. In 2019, in  
411 situ observations from both  
412 July and August confirm the  
413 conclusion from the satellite data  
414 that the transect area had larger  
415 Chl-a concentrations in August  
416 than in July. In particular, a  
417 patch of high chlorophyll in the  
418 mid-shelf between  $40.2^\circ\text{N}$  and  
419  $40.7^\circ\text{N}$  to the immediate west  
420 of the transect was present in  
421 August 2019, likely resulting from  
422 the observed *Hemiaulus* bloom.

### 411 3.2 Physical properties

412 During the NES-LTER summer 2019  
413 cruise, SST was higher than during  
414 most of the other summer cruises  
415 in the mid-shelf region (Table 2).  
416 Furthermore, SST in summer 2019  
417 on the outer-shelf region in particular  
418 was substantially higher than on any  
419 other summer cruise (Fig. 5a).  
420 Notably, the 2019 cruise occurred  
421 later in the summer season (August)  
422 than the NES-LTER cruises in other  
423 years (July). Along the NES-LTER  
424 transect specifically, SST in July  
425 2019 was lower than in August 2019  
426 and was similar to other years. In  
427 general, monthly-averaged satellite  
428 SST data in the broader NES region  
429 usually show lower SST values in  
430 July compared to August (2018,  
431 2020-2022) (Fig. S2). Interestingly,  
432 however, in summer 2019, the  
433 monthly averaged satellite data  
434 actually show higher SST in July,  
435 because of impingement of a Gulf  
436 Stream warm-core ring on the shelf  
437 edge (Zhang et al., 2023) and the  
438 subsequent onshore intrusion of the  
439 ring water in July 2019. The fact  
440 that monthly averaged satellite  
441 SST was higher in July than August  
442 but the local NES LTER transect data  
443 shows temperature higher in August  
444 than July suggests that the high SST  
445 observed during late August 2019  
446 reflected an ephemeral event and not  
447 a mean condition during that month.  
448 During the NES-LTER August 2019  
449 cruise, surface salinity was lower  
450 than on 2018, 2021, and 2022  
451 summer cruises, but similar to  
452 surface salinity during the July 2020  
453 cruise (Fig. 5b) and to salinities  
454 observed in July 2019 along the  
455 NES-LTER transect. Despite the NES-  
456 LTER summer 2019 cruise being in a  
457 specific week of August and the  
458 conditions suggesting an ephemeral  
459 event, for simplicity, we will refer  
460 to it as August 2019 in this paper.

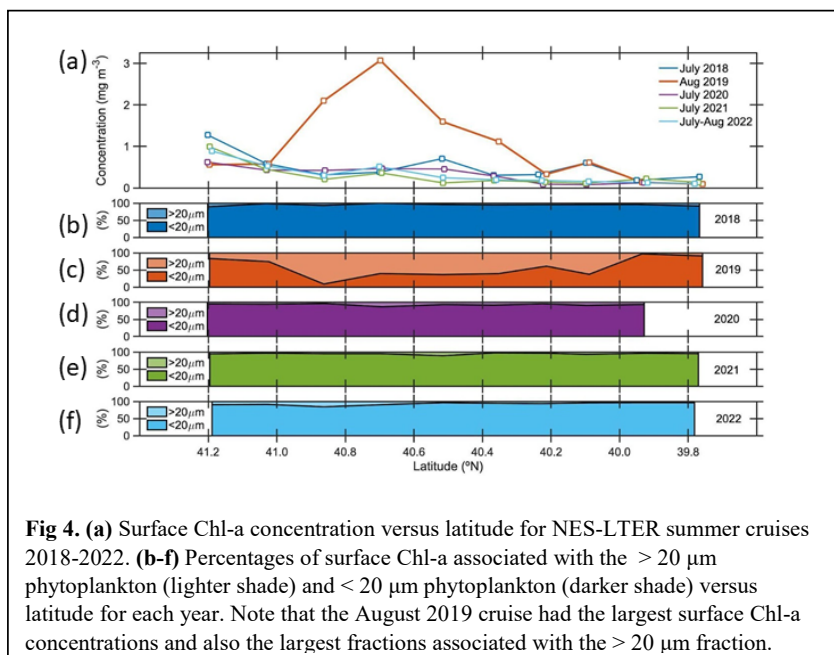


**Fig 4.** (a) Surface Chl-a concentration versus latitude for NES-LTER summer cruises 2018-2022. (b-f) Percentages of surface Chl-a associated with the  $> 20 \mu\text{m}$  phytoplankton (lighter shade) and  $< 20 \mu\text{m}$  phytoplankton (darker shade) versus latitude for each year. Note that the August 2019 cruise had the largest surface Chl-a concentrations and also the largest fractions associated with the  $> 20 \mu\text{m}$  fraction.

428 **Table 2.** Averages ( $\pm$  standard error) of surface mixed layer characteristics (productivity values integrated through the surface mixed layer; physical conditions,  
429 nutrients, and Chl-a concentrations from the surface) in the mid-shelf region measured during NES-LTER summer cruises for each year and overall averages  
430 from NES-LTER winter cruises 2018-2022 in the mid-shelf waters of the transect. The NPP average in 2018 (\*) was calculated based on the phytoplankton  
431 growth rate since direct NPP measurements were not available for this year. The standard error for 2020 NPP reflects the triplicate values from one station rather  
432 than multiple mid-shelf stations. The winter averages reflects mean of data collected in winters of 2018-2022.

	NCP ( $\mu\text{mol O}_2$ $\text{m}^{-2}\text{d}^{-1}$ )	GOP ( $\mu\text{mol O}_2$ $\text{m}^{-2}\text{d}^{-1}$ )	NCP/ GOP	NPP ( $\text{mg C}$ $\text{m}^{-2}\text{d}^{-1}$ )	Phyto- plankton growth rate ( $\text{d}^{-1}$ )	Micro- zoopl grazing ( $\text{d}^{-1}$ )	Temp- erature ( $^{\circ}\text{C}$ )	Salinity	Hemian- has Carbon ( $\mu\text{g L}^{-1}$ )	Chl-a ( $\text{mg m}^{-3}$ )	% Chl-a > 20 $\mu\text{m}$	Silicate ( $\mu\text{mol L}^{-1}$ )	Phosphate ( $\mu\text{mol L}^{-1}$ )
Summer	28.8	160	0.18	* 324	1.12	0.19	21.44	32.71	0.002	0.43	0.02	1.9	0.11
	$\pm 0.2$	$\pm 10$	$\pm 0.01$	$\pm 20$	$\pm 0.11$	$\pm 0.03$	$\pm 0.01$	$\pm 0.01$	$\pm 0.002$	$\pm 0.10$	$\pm 0.006$	$\pm 0.3$	$\pm 0.01$
<b>2019</b>	<b>28.8</b>	<b>110</b>	<b>0.24</b>	<b>398</b>	<b>0.20</b>	<b>0.17</b>	<b>24.29</b>	<b>31.83</b>	<b>28.4</b>	<b>1.97</b>	<b>1.37</b>	<b>0.27</b>	<b>0.025</b>
	$\pm 0.2$	$\pm 9$	$\pm 0.09$	$\pm 213$	$\pm 0.17$	$\pm 0.04$	$\pm 0.01$	$\pm 0.001$	$\pm 1.3$	$\pm 0.59$	$\pm 0.43$	$\pm 0.5$	$\pm 0.02$
2020	11.3	100	0.13	225	0.80	0.22	23.88	31.80	0.00	0.40	0.03	1.4	0.085
	$\pm 0.1$	$\pm 7$	$\pm 0.01$	$\pm 4$	$\pm 0.10$	$\pm 0.09$	$\pm 0.02$	$\pm 0.002$	$\pm 0.00$	$\pm 0.06$	$\pm 0.01$	$\pm 0.5$	$\pm 0.10$
2021	8.4	104	0.09	81	0.83	0.51	22.61	33.17	0.001	0.22	0.01	0.75	0.00
	$\pm 0.05$	$\pm 26$	$\pm 0.01$	$\pm 10$	$\pm 0.64$	$\pm 0.25$	$\pm 0.02$	$\pm 0.01$	$\pm 0.001$	$\pm 0.07$	$\pm 0.004$	$\pm 0.4$	$\pm 0.00$
2022	3.8	40	0.07	191	0.31	0.11	24.46	32.53	0.003	0.32	0.03	0.42	0.06
	$\pm 0.1$	$\pm 5$	$\pm 0.01$	$\pm 10$	$\pm 0.1$	$\pm 0.05$	$\pm 0.01$	$\pm 0.01$	$\pm 0.003$	$\pm 0.10$	$\pm 0.02$	$\pm 0.18$	$\pm 0.06$
Winter	All	5.1	101	0.11	464	0.30	0.24	6.131	32.786	0.018	2.17	1.56	1.7
	yrs	$\pm 0.1$	$\pm 20$	$\pm 0.04$	$\pm 63$	$\pm 0.04$	$\pm 0.05$	$\pm 0.007$	$\pm 0.002$	$\pm 0.006$	$\pm 0.16$	$\pm 0.14$	$\pm 0.5$

433





434

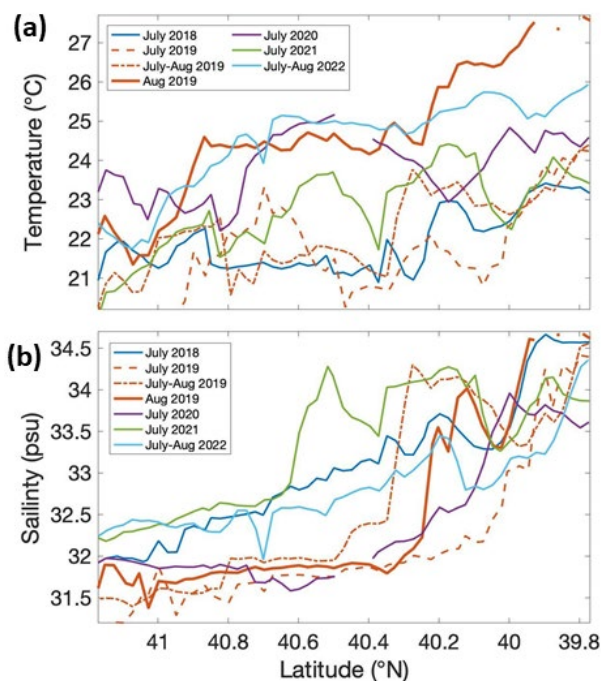


**Fig 5.** (a) Temperature and (b) salinity 5 m below the surface versus latitude for NES-LTER summer cruises (2018-2022) and the SPIROPA and OTZ summer 2019 cruises. For clarity, the values are averaged in 0.025 degree latitude bands when there were multiple occupations of the same region.

458

459

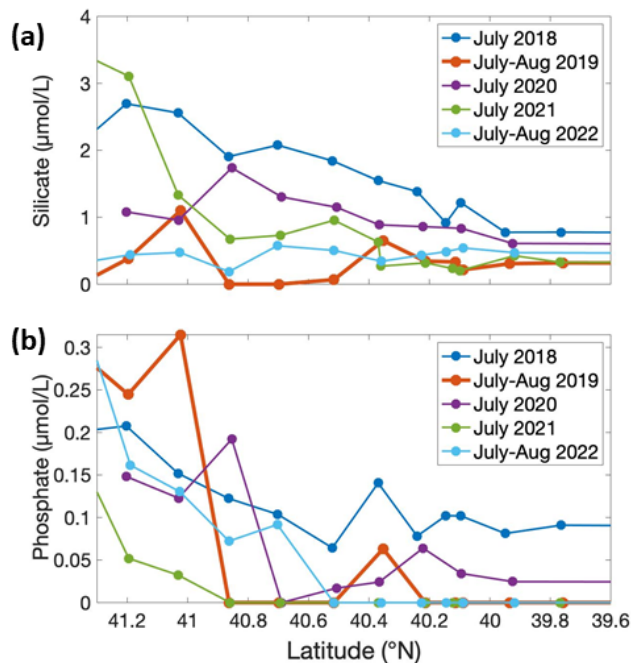


**Fig 6.** (a) Silicate and (b) phosphate concentrations (in  $\mu\text{mol/L}$ ) in the upper 12 m of the water column for NES-LTER summer cruises (2018-2022).



### 483 3.3 Nutrients

484 Nutrient concentrations differed between the August 2019 cruise and other summer cruises. Specifically, phosphate  
485 and silicate concentrations in surface waters were lower in August 2019 compared to other summers (Table 2). In  
486 other summers, silicate decreased with distance from shore, but in 2019, silicate was depleted between 41°N and  
487 40.4 °N (Fig. 6a) coincident with the location of the *Hemiaulus* bloom. Additionally, higher levels of silicate were  
488 found around depths of 50 m to 140 m in August 2019 than during other summer NES-LTER cruises (Fig. S3),  
489 which may be associated with diatoms that had sunk and were starting to be remineralized, releasing silicate back  
490 into the water column. Surface water phosphate concentrations in August 2019 were depleted south of 41° N (Fig.  
491 6b). However, low concentrations of phosphate were also found in summers of 2020 and 2021. Lastly, nitrate +  
492 nitrite concentrations were close to the detection level in the surface samples for all summer cruises except a few  
493 stations in 2018. Ammonium levels are not discussed because the samples were frozen at sea and thus may not be  
494 reliable; additionally, ammonium levels showed no clear relationship over the transect cruises.  
495

### 496 3.4 Productivity and grazing rates

497 In August 2018 NCP was  
498 elevated in the mid-shelf waters,  
499 coincident with the location of the  
500 *Hemiaulus* bloom (Fig. 1). NCP  
501 peaked in the first half of the  
502 cruise and decreased during the  
503 second half, supporting the earlier  
504 supposition that the *Hemiaulus*  
505 bloom was likely in decline.  
506 Additionally the area of  
507 maximum NCP moved shoreward  
508 in the second half of the cruise.  
509 The high NCP was primarily  
510 constrained to the main longitude  
511 sampling line and usually did not  
512 extend, at least at those points in  
513 time, spatially off the main  
514 transect.

515 During August 2019,  
516 waters with high carbon  
517 concentrations of *Hemiaulus*  
518 showed higher rates of NCP (Fig.  
519 7a), NCP/GOP (Fig. 7b), GOP  
520 (Fig. 7c), and NPP (Fig. 7d)  
521 compared to these rates at mid-  
522 shelf waters in most other years.  
523 More specifically, the mid-shelf  
524 waters where *Hemiaulus* was  
525 present in Aug 2019 displayed  
526 NCP values approximately 2.5 to  
527 9 times larger than in the same  
528 mid-shelf latitudes in summers of 2020-22 (Table 2). Furthermore, we observed a correlation between NCP and  
529 *Hemiaulus* carbon between Aug 21 and Aug 23 (Fig. 8;  $R^2 = 0.54$ ,  $p < 0.001$ ). The patchiness of the diatom bloom  
530 corresponded to the patchiness in NCP. Additionally, one can see that the cooler shelf water was associated with  
531 higher abundances of *Hemiaulus* than the warmer slope water (Fig. 8), suggesting a water mass dependence on  
532 the location of the *Hemiaulus* bloom. Thus the patchiness in the bloom and NCP is likely a result of the ship crossing  
533 different water masses.

534 GOP rates were higher by a factor of 1.1 in waters with the *Hemiaulus* bloom in 2019 than during the  
535 summers of 2020-21; GOP rates were much higher in August 2019 than in summer of 2022 by a factor of 2.75.

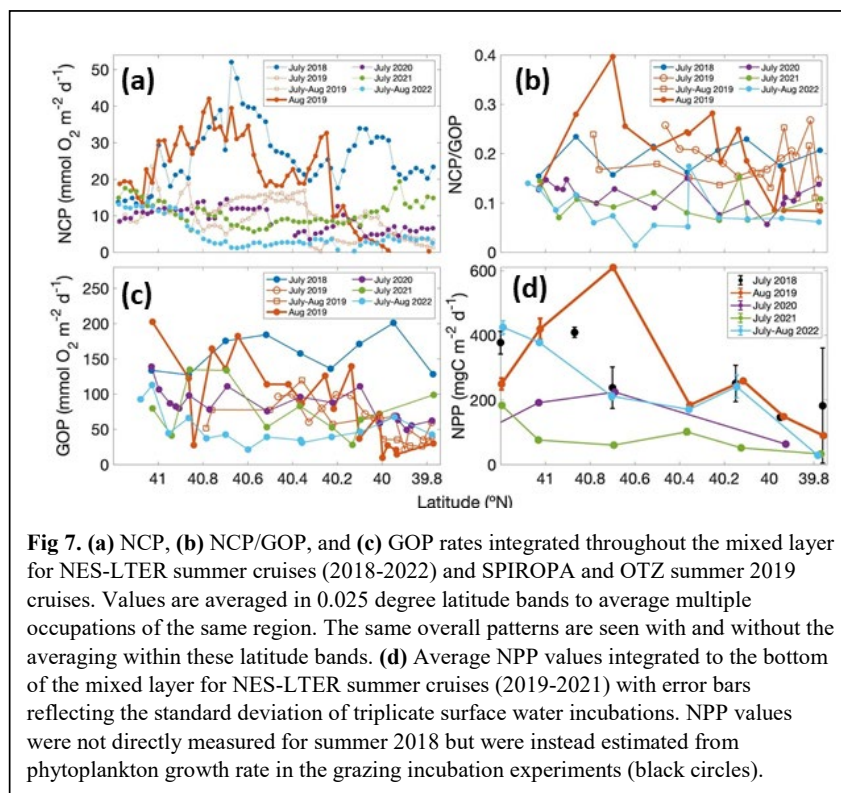


**Fig 7.** (a) NCP, (b) NCP/GOP, and (c) GOP rates integrated throughout the mixed layer for NES-LTER summer cruises (2018-2022) and SPIROPA and OTZ summer 2019 cruises. Values are averaged in 0.025 degree latitude bands to average multiple occupations of the same region. The same overall patterns are seen with and without the averaging within these latitude bands. (d) Average NPP values integrated to the bottom of the mixed layer for NES-LTER summer cruises (2019-2021) with error bars reflecting the standard deviation of triplicate surface water incubations. NPP values were not directly measured for summer 2018 but were instead estimated from phytoplankton growth rate in the grazing incubation experiments (black circles).

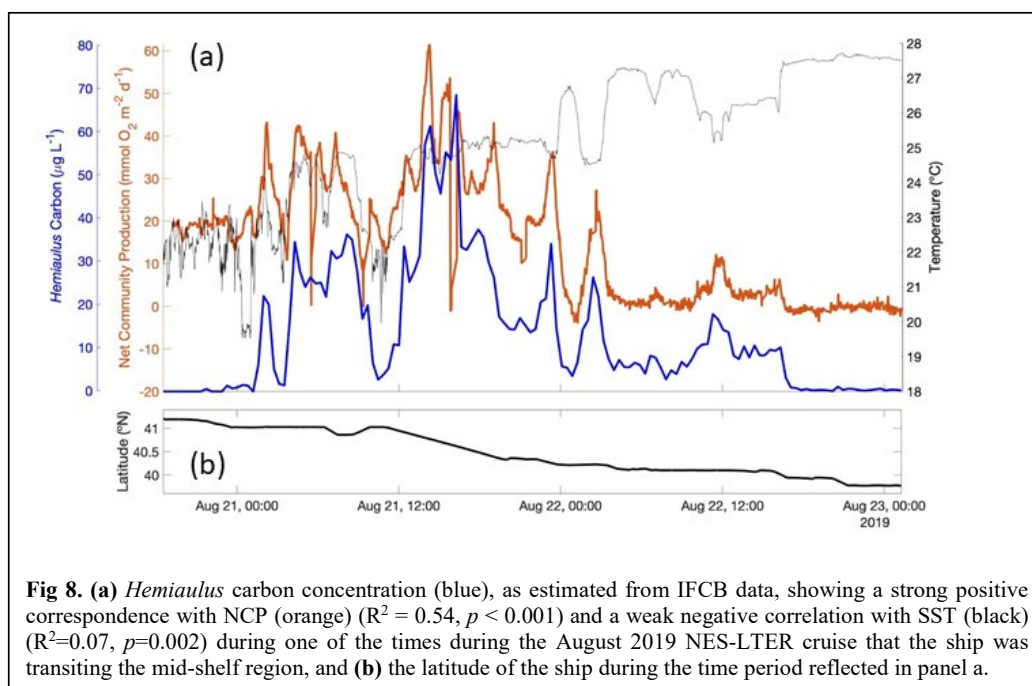


**Fig 8.** (a) *Hemiaulus* carbon concentration (blue), as estimated from IFCB data, showing a strong positive correspondence with NCP (orange) ( $R^2 = 0.54$ ,  $p < 0.001$ ) and a weak negative correlation with SST (black) ( $R^2=0.07$ ,  $p=0.002$ ) during one of the times during the August 2019 NES-LTER cruise that the ship was transiting the mid-shelf region, and (b) the latitude of the ship during the time period reflected in panel a.

536 Additionally, during August 2019, NPP rates were generally higher throughout the cruise compared to rates from  
537 July 2020–2022 and estimates for July 2018. Within the region that corresponds directly with the location of the  
538 *Hemiaulus* bloom, NPP rates in 2019 were ~1.5 - 2.5 times higher than NPP rates during other summer cruises. (Fig.  
539 7d; Table 2). More specifically, NPP at 40.7  $^{\circ}\text{N}$  was approximately double the NPP measured in 2020 and more than  
540 double the rate measured in 2021. Furthermore, at 40.4  $^{\circ}\text{N}$ , NPP in 2019 was about 40% higher than in 2021 (no  
541 data for this station in 2020) (Fig. 7d).

542 A larger difference between NCP in the various summers than between GOP in the summers suggests that  
543 the increase in NCP in August 2019 was due to both increased photosynthesis and decreased community respiration.  
544 As a first approach, we calculated autotrophic respiration and heterotrophic respiration, to show that autotrophic  
545 respiration was lower than average in August 2019 ( $R_A = 308 \text{ mgC m}^{-2}\text{d}^{-1}$  in August 2019 versus  $496 \text{ mgC m}^{-2}\text{d}^{-1}$   
546 average for the other summers). This approach also showed that heterotrophic respiration was higher than average in  
547 August 2019 ( $431 \text{ mgC m}^{-2}\text{d}^{-1}$  in August 2019 versus  $247 \text{ mgC m}^{-2}\text{d}^{-1}$  average for the other summers). NCP, GOP,  
548 and NCP/GOP rates in summer 2018 were comparable to these rates in August 2019 (discussed below in section  
549 4.1).

550 Since the summer 2019 NES-LTER cruise occurred in the middle of August rather than in mid to late July  
551 as was typical for most other summers, the physical conditions were inherently different in 2019. We compared  
552 NCP and GOP data (NPP not available) from two earlier cruises in summer 2019 (cruise details in Table 1) whose  
553 stations overlapped with those of the LTER cruise (Fig. 7). These cruises occurred before the *Hemiaulus* bloom and  
554 their IFCB records did not show high abundance of *Hemiaulus* ( $< 1 \mu\text{gC L}^{-1}$ ), although it was detected at that time.  
555 These two July 2019 cruises had much lower NCP rates compared to August 2019 NCP rates, specifically with rates  
556 similar to those observed in summer 2020-22 NES-LTER transect cruises (Fig. 7a & b). Together, these data suggest  
557 that higher production rates were uniquely tied to the presence of *Hemiaulus* rather than representing deviations in  
558 timing or environmental conditions.

559 The ratio of protistan grazing to phytoplankton growth rates provides an estimate of the percent of primary  
560 production (%PP) consumed by microzooplankton (Fig. 9). In contrast to typical summer conditions ( $> 0.6 \text{ d}^{-1}$ ,  
561 Table 2), during August 2019, phytoplankton growth rates during the *Hemiaulus* bloom were low ( $< 0.2 \text{ d}^{-1}$ , Table  
562 2), likely because the bloom was near its end, with most of the primary production consumed by microzooplankton  
563 (%PP = 84%, Table 2). Thus in August 2019, the phytoplankton growth and microzooplankton grazing were well  
564 coupled (though only in the part of the transect where *Hemiaulus* bloomed), like typical winter conditions, when the

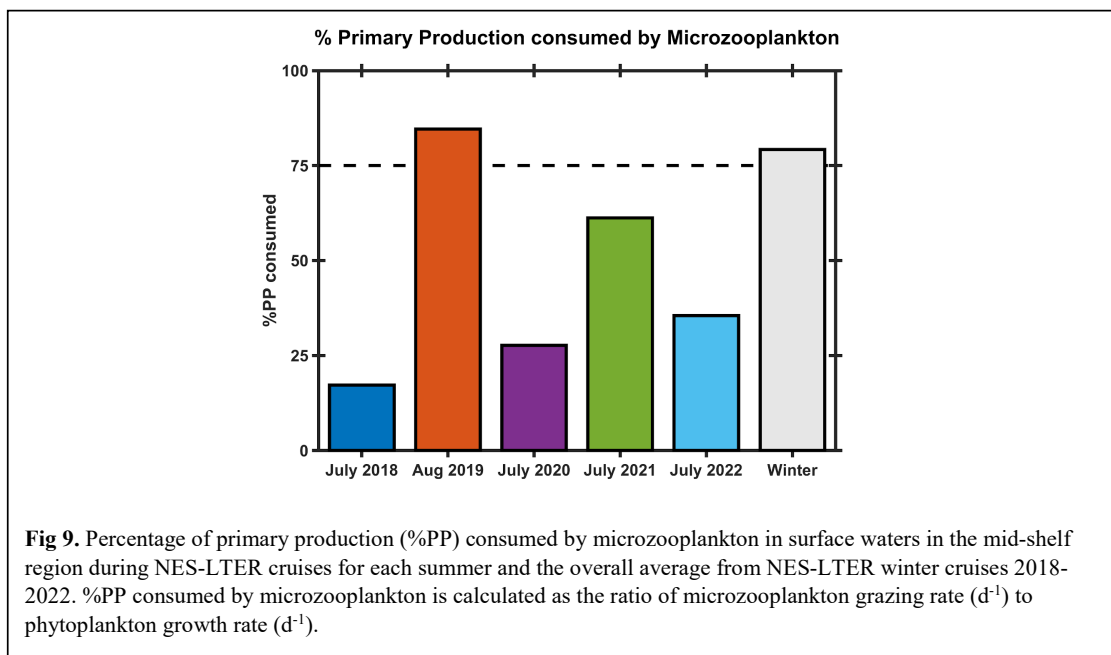


**Fig 9.** Percentage of primary production (%PP) consumed by microzooplankton in surface waters in the mid-shelf region during NES-LTER cruises for each summer and the overall average from NES-LTER winter cruises 2018-2022. %PP consumed by microzooplankton is calculated as the ratio of microzooplankton grazing rate ( $d^{-1}$ ) to phytoplankton growth rate ( $d^{-1}$ ).

565 phytoplankton community structure is dominated by large cells, instead of the decoupling typically observed in most  
566 summer conditions dominated by picoplankton (Marrec et al., 2021). We note that coupling between phytoplankton  
567 growth and microzooplankton grazing was occasionally observed during other summer cruises, but mostly in inner-  
568 shelf waters (except one mid-shelf station in July 2021). Overall, most of the primary production during the  
569 *Hemiaulus* bloom was grazed by microzooplankton indicating high trophic transfer efficiency from phytoplankton to  
570 microzooplankton.

## 571 4 Discussion

### 572 4.1 Change in community composition altering biological rates

573 A bloom of *Hemiaulus* has not been observed on any previous NES-LTER cruise and to our knowledge,  
574 has not been reported in the broader NES region before. Additionally, only in August 2019, compared to summers  
575 2018 and 2020-22, was most of the Chl-a associated with the  $> 20 \mu m$  size fraction. Thus, the presence of the diatom  
576 bloom found in August 2019 is a major change in phytoplankton composition observed in this region of the NES  
577 that led to large changes in productivity rates and to the coupling between phytoplankton growth and grazing.

578 It is likely that the nitrogen-fixing symbionts in *Hemiaulus* allowed the diatom to thrive in the stratified,  
579 low nutrient surface waters of the summer shelf. This is supported by phosphate being drawn down to levels below  
580 detection only in August 2019; the nitrogen-fixing symbionts in the *Hemiaulus* likely made phosphate a limiting  
581 factor for growth (Tang et al., 2020) in August 2019 whereas nitrate limitation is typical for NES summer  
582 conditions. Additionally, silicate is especially important for diatoms because it is required for formation of their cell  
583 frustules. Moreover, previous studies show that the availability of dissolved silica seems to be an important control  
584 for many diatom-diazotroph blooms by affecting the growth rate and size of the diatom's frustules (Kemp and  
585 Villareal, 2013, Spitzer, 2015). The observed depletion of silicate and phosphate in the surface water during the  
586 August 2019 cruise suggests that, at the time of the cruise, the *Hemiaulus* bloom might have been on the decline.  
587 The very low phytoplankton growth rates might also support the idea that the bloom had peaked but also might be  
588 attributed to the inverse relationship between phytoplankton cell size and growth rate (e.g. Finkel et al., 2010). The  
589 higher levels of silicate observed at depth in August 2019 are likely due to the *Hemiaulus* sinking out of the euphotic  
590 zone and their frustules re-mineralizing at depth, which would release the silicate—and other nutrients—back into the



591 water (Twining et al., 2014). In any case, it appears the *Hemiaulus* population could have been limited by phosphate,  
592 silicate, or both.

593 The strong coherence between the high spatial resolution data on *Hemiaulus* carbon concentrations and  
594 NCP (Fig. 8), as well as the other data presented here and a clear potential mechanism, strongly support the idea that  
595 the high productivity rates observed in August 2019 are directly due to the presence of *Hemiaulus*. In particular, the  
596 high NCP rates observed during the August 2019 NES-LTER cruise and their overlap with the location of the  
597 diatom bloom, suggest a high export ecosystem developed due to *Hemiaulus*' influence on productivity and  
598 biological rates. Here we are defining export as a flux away from the local biological production compartment,  
599 which can include losses of carbon (or oxygen) to depth or transfer to higher trophic levels. While the *Hemiaulus*  
600 bloom slightly increased total photosynthesis, as seen from the GOP rates, the bloom presence affected NCP, and  
601 thus by extension, export production, even more, potentially due to the large size of *Hemiaulus* cells and chains. The  
602 NCP/GOP ratio in August 2019 was double the ratio observed in the summers 2020-22 (Table 2). Other studies have  
603 shown links between variations in NCP/GOP and changes in planktonic community composition (Palevsky et al.,  
604 2016). Bigger phytoplankton cells sink faster than small ones, making them less likely to be grazed before sinking  
605 out of the euphotic zone, allowing for a higher export efficiency. Hence, the NES-LTER summer of 2019 cruise  
606 appears to represent a high carbon export efficiency system.

607 Not only did NCP and GOP rates change because of the *Hemiaulus* bloom, but so did NPP, phytoplankton  
608 growth rates, chl-a concentrations, and the trophic transfer efficiency within the planktonic food web. The presence  
609 of *Hemiaulus* in the mid-shelf region led to higher NPP rates during August 2019 compared to all other observed  
610 summers in the mid-shelf region of the NES (Fig. 7). High NPP rates associated with diatom blooms have been  
611 observed in other systems such as on the Eastern Bering Shelf (Lomas et al., 2012) and in the Gulf of California  
612 (Puigcorbe et al., 2015). In particular, diatom-diazotroph associations such as *Hemiaulus-Richelia* are known to  
613 significantly increase NPP (Gaysina et al., 2019). For example, Tang et al. (2020) reported a high contribution of  
614 nitrogen fixation to NPP off the coast of New Jersey during their 2015-2016 survey in the Western North Atlantic.  
615 Even though high NPP was associated with the location of the *Hemiaulus* bloom in our study, phytoplankton growth  
616 rates were low ( $<0.2 \text{ d}^{-1}$ ). This decoupling between NPP and growth was likely due to the order of magnitude higher  
617 chl-a concentrations observed during August 2019 ( $1.37 \mu\text{g L}^{-1}$ ) compared to other summers ( $0.01 - 0.03 \mu\text{g L}^{-1}$ ;  
618 Table 2) since NPP is roughly the product of phytoplankton growth and biomass (Marchetti et al. 2009). Thus,  
619 although growth rate was low, biomass was so high that NPP was also high. Furthermore, most of the primary  
620 production was directly consumed by microzooplankton, which we have not observed during any other summer  
621 NES-LTER cruise, suggesting the presence of *Hemiaulus* led to more efficient trophic transfer during August 2019.  
622 While conditions with high NCP (i.e. low community respiration) and high grazing pressure as observed in August  
623 2019 may seem counterintuitive, they are not contradictory since grazing cannot be equated with respiration. First,  
624 much of respiration is bacterial and therefore not reflected by the grazing rates (Robinson and Williams, 2005).  
625 Second, it has been observed that after starvation, protozoan grazers increase their organic matter production by  
626 accumulating lipids and increasing their cell size (Anderson and Menden-Deuer, 2017, Morison et al., 2020). Thus,  
627 high grazing could suggest a buildup of organic matter through secondary production, which is consistent with the  
628 higher than average microzooplankton biomass and would be reflected as large NCP. Third, microzooplankton can  
629 produce fecal pellets (Buck and Newton, 1995), removing carbon from the system without respiration and thus lead  
630 to high NCP. The dominant presence, and slow growth, of large *Hemiaulus* cells within the phytoplankton  
631 community was likely a main factor promoting the higher trophic transfer efficiency from phytoplankton to  
632 microzooplankton, as is typical during winter (Marrec et al., 2021).

633 Interestingly, NCP and GOP values in summer 2018 were similar to those in August 2019 (Table 2, Fig. 7)  
634 and also much higher than during subsequent summers (2020-2022), in spite of no *Hemiaulus* being present in  
635 summer 2018. Additionally, the ratio of NCP/GOP in summer of 2018 was also significantly larger than in 2020-22  
636 (Fig. 7). Remote sensing shows an elevated Chl-a patch (less concentrated than the patch in August 2019) in  
637 summer 2018 west of the transect that could be the driving factor behind the high NCP and GOP values (Fig.  
638 S1). The summer of 2018 was dominated by small phytoplankton similar to observations in summers of 2020 and  
639 2021, although the summer of 2018 had a particularly high concentration of dinoflagellates over parts of the shelf.  
640 The summer 2018 data did not show an increase in trophic transfer efficiency due to coupled microzooplankton  
641 grazing and phytoplankton growth nor did it show increased NPP. The high NCP in summer 2018 could be due to a  
642 variety of environmental (biotic and abiotic) factors that were different from other cruises. For example, in the  
643 summer of 2018, saline waters from offshore intruded much farther inshore than during most of the other summers  
644 and these high-salinity mid-shelf waters were particularly productive (Mehta, 2022). Additionally, correspondence  
645 was seen between NCP and dinoflagellate biomass in summer 2018, although not as significantly as was seen with  
646 the *Hemiaulus* and NCP in 2019 (Aldrett, 2021). Thus, this study shows that a change in community composition,





647 such as the *Hemiaulus* bloom in August 2019, can dramatically change the productivity rates of the ecosystem and  
648 yet productivity rates can also be similarly high with a very different phytoplankton community structure.

#### 649 4.2 Aggregate vs Compositional Variability

650 The changes in community composition, productivity rates, and chlorophyll in August 2019 compared to the other  
651 summers shed interesting light on the question of synchrony or compensation between aggregate and compositional  
652 variability at the NES-LTER site (Micheli et al., 1999, Shoemaker et al., 2022). The resilience of an ecosystem may  
653 be related to the compensation or synchrony  
654 between different types of variability  
655 (Lindegren et al., 2016). During August 2019,  
656 the phytoplankton composition in the NES  
657 changed dramatically due to the bloom of the  
658 diatom *Hemiaulus*. This change was  
659 associated with increases in Chl-a, higher  
660 productivity rates, tighter coupling between  
661 microzooplankton grazing and phytoplankton  
662 growth, and increases in export efficiency.  
663 These latter terms are all metrics of aggregate  
664 properties and thus this bloom event exhibited  
665 high compositional and high aggregate  
666 variability compared to the ecosystem in July  
667 of 2020-22. Thus, during this event, a change  
668 in compositional variability (e.g., the change  
669 in phytoplankton community composition)  
670 was synchronous with a change in aggregate  
671 variability. However, when NCP rates are  
672 compared from summer 2018 to summer  
673 2019, the compositional variability is still  
674 quite different (*Hemiaulus* in 2019, mostly  
675 small phytoplankton in 2018) but the  
676 aggregate variability in terms of NCP is the  
677 same in both years – thus comparing those  
678 two summers is a case where compositional  
679 variability changed and yet aggregate  
680 variability (at least for NCP) did not. Why  
681 does community composition sometimes  
682 affect NCP dramatically (i.e., August 2019 vs  
683 July of 2020-22) and sometimes it does not  
684 (July 2018)? Perhaps NCP is affected more by  
685 the abundance of certain species in the  
686 community rather than size distribution of the  
687 community. This concurrent investigation of  
688 plankton community composition and  
689 production rates within a well-studied  
690 ecosystem highlights how shifts in community  
691 size distribution can greatly affect  
692 productivity. However, it also shows that  
693 multiple factors change from year to year,  
694 leading to different effects.

#### 695 4.3 Origin of Bloom

696 The *Hemiaulus* bloom was likely more  
697 widespread than what was observed in the  
698 NES-LTER 2019 summer cruise. For

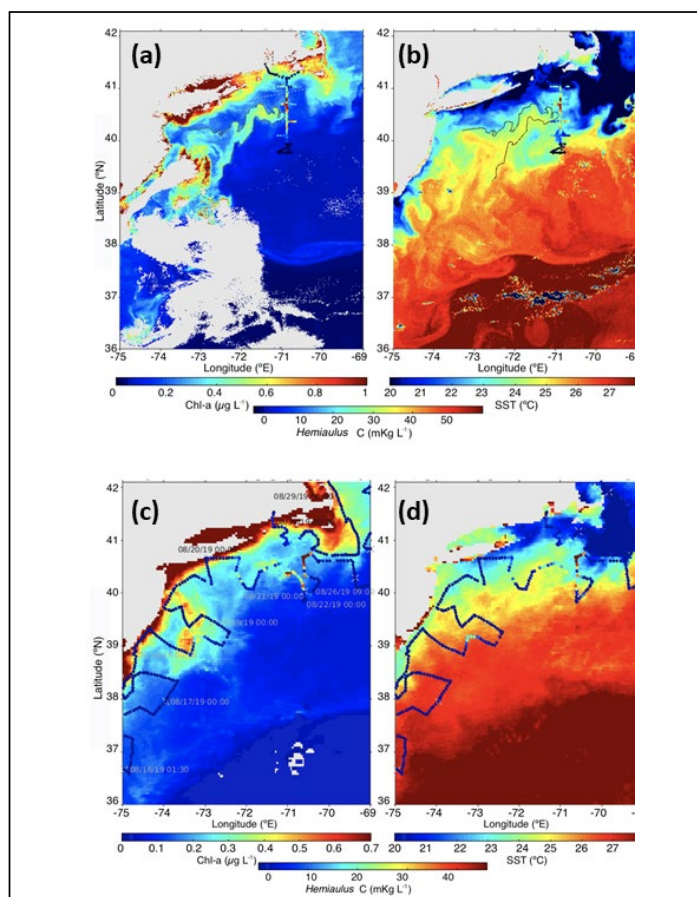


**Fig 10.** Snapshots of satellite-measured (a) Chl-a and (b) SST on 11 August 2019. The  $0.5 \mu\text{g L}^{-1}$  chlorophyll contour is plotted as a solid line. *Hemiaulus* carbon from underway surface samples during the NES-LTER Aug 2019 cruise is overlaid with colored dots. The monthly composite (c) Chl a and (d) SST for August 2019. *Hemiaulus* carbon from underway surface samples during ECOMON cruise GU1902 is overlaid with colored dots. Daily ship positions are indicated in the left panel. Animated versions of individual Chl a and SST images are available at: [http://science.whoi.edu/users/olga/outgoing/Aug\\_2019\\_chl/NEW\\_2019\\_Hemiaulus/](http://science.whoi.edu/users/olga/outgoing/Aug_2019_chl/NEW_2019_Hemiaulus/)

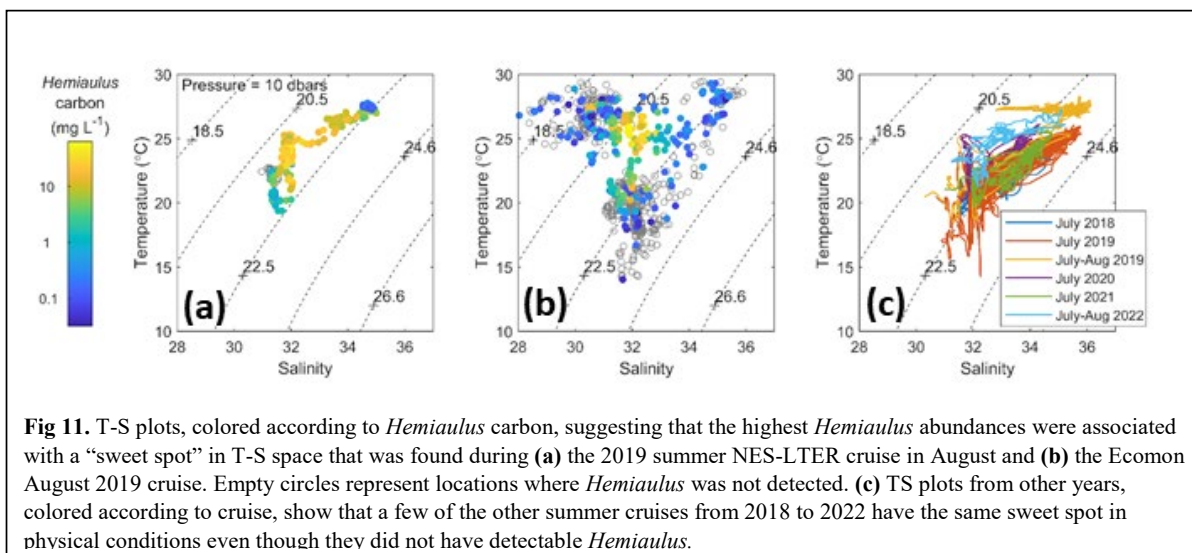


**Fig 11.** T-S plots, colored according to *Hemiaulus* carbon, suggesting that the highest *Hemiaulus* abundances were associated with a “sweet spot” in T-S space that was found during (a) the 2019 summer NES-LTER cruise in August and (b) the Ecomon August 2019 cruise. Empty circles represent locations where *Hemiaulus* was not detected. (c) TS plots from other years, colored according to cruise, show that a few of the other summer cruises from 2018 to 2022 have the same sweet spot in physical conditions even though they did not have detectable *Hemiaulus*.

699 example, satellite imagery from August 11 shows a filament of warm, high Chl-a waters oriented southwest-  
700 northeast and ending in the region where *Hemiaulus* was abundant (Fig. 10a & b); the advective continuity of the  
701 filament with the *Hemiaulus* patch suggests the filament may have had high *Hemiaulus* as well. Direct support for a  
702 widespread bloom comes from IFCB data collected on the NOAA EcoMon Cruise (GU1902) that occurred at a  
703 similar time as the August 2019 NES-LTER transect cruise. The IFCB data shows that *Hemiaulus* was present both  
704 farther east as well as to the southwest of where it was observed on the LTER transect cruise and that some of the  
705 points in the high chlorophyll filament observed from satellite chlorophyll contained *Hemiaulus* (Fig. 10c).

706 Backward particle trajectory analysis based on HF radar-measured sea surface velocities show that the  
707 water with high *Hemiaulus* biomass during the August 2019 transect cruise could have been advected from the  
708 inner-shelf around Narragansett Bay and Georges Bank rather than from the mid-shelf further south (Fig. S4). In  
709 particular, coastal upwelling probably brought the inner-shelf water into the mid-shelf transect area where it was  
710 observed to have high *Hemiaulus*. The salinity of the water with the high *Hemiaulus* biomass is consistent with the  
711 water having originated from the shelf. The water with high amounts of *Hemiaulus* carbon was associated with  
712 salinity ranging from 31.6 to 34 psu and temperatures of 22°C to 27°C (Fig. 11a & b). T-S plots of data from other  
713 years (Fig. 11c) suggest that several other summers also had similarly warm, low salinity water (in particular July of  
714 2020 and especially 2022) but interestingly *Hemiaulus* were not observed on those cruises.

715 Although multiple lines of evidence suggest that the water containing the high biomass of *Hemiaulus*  
716 initially originated from the inner-shelf, *Hemiaulus* is typically found in warm, low nutrient water – characteristics  
717 that are not present on the inner-shelf, where water is instead colder and often richer in nutrients. In this case, the  
718 inner-shelf water warmed as it was transported offshore and thus it reached temperatures warm enough for  
719 *Hemiaulus* to thrive by the time it reached the mid-shelf (the timing of warming is not known). But how did this  
720 inner-shelf water acquire *Hemiaulus* as it was transported offshore in August 2019? One possibility is that it was  
721 seeded by the warmer low nutrient surface slope and ring waters; in particular, these slope and ring waters  
722 were observed earlier in the summer of 2019 to have a small population of *Hemiaulus* that could have served as a  
723 seed population (Oliver et al., 2021). However, there is no evidence of surface transport from slope-water to the  
724 *Hemiaulus* patch. Another possibility is that *Hemiaulus* were already present in the deeper coastal water and then  
725 thrived as the deep water was mixed upward, warmed and reached the higher light surface waters. However, the  
726 vertical distributions of *Hemiaulus* (Fig. 3) do not support this hypothesis, since a deeper population was not  
727 observed. Thus, the reason *Hemiaulus* bloomed in 2019, and not in other years, remains a topic for future research  
728 and continued speculation. Future years of the NES-LTER program may shed light on the variable effects of  
729 disturbances, such as this *Hemiaulus* bloom, as more factors that lead to high or low export in summer are  
730 determined and explored.

## 731 5 Conclusions



732 An unusual bloom of the diatom genus *Hemiaulus* with nitrogen-fixing symbionts in the mid-shelf region of the  
733 Northeast U.S. shelf in August 2019 led to increases in NCP, GOP, NPP, higher export efficiency, and higher  
734 trophic transfer efficiency from phytoplankton to microzooplankton. Very tight coupling observed between  
735 kilometer-scale changes in NCP and the carbon biomass of *Hemiaulus* showed how substantial an effect the  
736 *Hemiaulus* bloom had on the aggregate variability of the Northeast U.S. shelf. While the source of the *Hemiaulus* on  
737 the inner-shelf remains unknown, the bloom was associated with warmer temperatures than usually observed on the  
738 shelf which may have been an important factor that facilitated the bloom when it was transported from the inner-  
739 shelf.

740 The *Hemiaulus* bloom, which was associated with warmer temperatures, was intriguing in that it led to  
741 unusually high productivity rates, increases in Chl-a concentrations, and tighter food-web coupling. While the warm  
742 SST may have contributed to the *Hemiaulus* bloom, the summer cruises of 2020 and 2022 also had anomalously  
743 high water temperatures, but relatively low (i.e., average summer) productivity rates and Chl-a were observed during  
744 those times. So, these summers of 2020 and 2022 had similar physical conditions to that of 2019, but no significant  
745 bloom was observed, and no high-carbon export system was present. Thus, higher temperatures are not enough to  
746 explain higher productivity rates, a shift in community composition is also necessary. A mixture of the right physical  
747 conditions and community composition, like this special case of 2019, are needed for a high-carbon export system to  
748 be supported on the mid-shelf during summer.

749 With climate change, the oceans are warming at a rapid rate, and are likely moving towards warmer more  
750 stratified conditions (e.g., lower nitrate stock in surface waters) (Li et al., 2020) which may lead to less productivity  
751 and thus lower export efficiencies. However, these conditions may also lead to unusual phytoplankton composition  
752 as species shift and the work presented here shows that those unusual events can lead to large locally and  
753 episodically enhanced productivity and export; despite the ecosystem commonly becoming nitrate-limited during the  
754 summer season, an intense phytoplankton bloom in summer occurred due to a symbiotic diatom-diazotroph  
755 relationships. These observations lead to further questions about how the NES ecosystem is responding to the effects  
756 of climate change such as enhanced stratification. Monitoring future disturbances and their effects will provide new  
757 insights into relationships, mechanisms, and patterns of composition and productivity that may be only occasionally  
758 occurring now but are likely more prevalent in the future.

## 759 6 Data Availability

760 All in situ data are available at the EDI data repository. In particular, the raw gas tracer data used for calculating  
761 NCP and GOP is available at  
762 <https://portal.edirepository.org/nis/mapbrowse?packageid=knb-lter-nes.6.2>. The calculated rates of NCP data is  
763 accessible at <https://portal.edirepository.org/nis/mapbrowse?packageid=knb-lter-nes.7.2>  
764 and <https://portal.edirepository.org/nis/mapbrowse?packageid=knb-lter-nes.15.2>. NPP data is available at  
765 <https://portal.edirepository.org/nis/metadataviewer?packageid=knb-lter-nes.16.4>. Grazing rate data is available at  
766 <https://portal.edirepository.org/nis/mapbrowse?packageid=knb-lter-nes.5.1>. Chlorophyll data is available at  
767 <https://portal.edirepository.org/nis/mapbrowse?packageid=knb-lter-nes.8.1>. IFCB data is available at  
768 <https://portal.edirepository.org/nis/mapbrowse?packageid=knb-lter-nes.9.1> and on the IFCB dashboard  
769 at [https://ifcb-data.whoi.edu/timeline?dataset=NESLTER\\_transect](https://ifcb-data.whoi.edu/timeline?dataset=NESLTER_transect).

770  
771 The MODIS SST and chlorophyll snapshot data were produced by NASA Goddard Space Flight Center, Ocean  
772 Ecology Laboratory, Ocean Biology Processing Group, and the data are publicly available at  
773 <https://oceancolor.gsfc.nasa.gov/>. The 8-day composite data were retrieved from the public-accessible University of  
774 Delaware ERDDAP server (<https://basin.ceoe.udel.edu/erddap/index.html>) maintained by the Ocean Exploration,  
775 Remote Sensing and Biogeography Laboratory led by Dr. Matthew Oliver at University of Delaware. The HF radar-  
776 measured sea surface velocity data in July-August 2019 was obtained from the public-accessible Rutgers University  
777 Center for Ocean Observing Leadership ERDDAP server (<http://hfr.marine.rutgers.edu/erddap/griddap/>).

## 778 Author Contribution

779 SAC, RHRS, ZOS, and DA measured and calculated rates of productivity from gas tracers. SMD and PM measured  
780 grazing rates. TAR and DNF measured and calculated rates of net primary productivity from bottle incubations.  
781 HMS, ETC and EEP imaged and quantified phytoplankton abundances. DJM and WGZ analyzed remote sensing



782 data. Everyone participated in study design. SAC and RHRS prepared the manuscript with contributions from all co-  
783 authors.

#### 784 **Competing Interests**

785 The authors declare that they have no conflict of interest.

#### 786 **Acknowledgements**

787 This work was funded by the National Science Foundation (LTER-1655686, OCE-1657489, OCE-1657803, OCE-  
788 2227425). S. A. Castillo Cieza was supported by the Clara Boothe Luce Fellowship program at Wellesley College.  
789 We are thankful for the scientific input, discussions and help from the entire NES-LTER science team. We are  
790 grateful to the Captain and crew of the *R/V Endeavor*. We recognize the contributions of Kevin Cahill (WHOI), who  
791 ran some of the samples for triple oxygen isotope measurement, Elizabeth Lambert (Wellesley College) and Helene  
792 Alt (Wellesley College) who helped collect some of the EIMS data, and Danielle Aldrett (Wellesley College) for  
793 doing some initial analysis on connections between the IFCB and NCP data. We thank NES-LTER data manager  
794 Stace Beaulieu and Kate Morkeski (WHOI) for their help in data management. We thank URI-GSO undergraduate  
795 and graduate students and postdocs who helped collect samples and conduct experiments to obtain chl-*a*  
796 concentrations, and phytoplankton growth and microzooplankton grazing rates. We thank Sam Setta for pointing out  
797 *Hemiaulus* in IFCB images during the cruise. DJM gratefully acknowledges NSF support of the SPIROPA program,  
798 and technical assistance by Olga Kosnyrev in satellite data analysis and visualization.

#### 799 **References**

- 800 Aldrett, D. 2021. *Understanding the relationship between photosynthetic organisms and oceanic*  
801 *productivity in the Northeast U.S. Shelf*. BA undergraduate thesis, Wellesley College.
- 802 Anderson, S. R. & Menden-Deuer, S. 2017. Growth, Grazing, and Starvation Survival in Three  
803 Heterotrophic Dinoflagellate Species. *Journal of Eukaryotic Microbiology*, 64, 213-225.
- 804 Armbrust, E. V. 2009. The life of diatoms in the world's oceans. *Nature*, 459, 185-192.
- 805 Barkan, E. & Luz, B. 2011. The relationships among the three stable isotopes of oxygen in air, seawater  
806 and marine photosynthesis. *Rapid Communications in Mass Spectrometry*, 25, 2367-2369.
- 807 Boyd, P. W., Claustre, H., Levy, M., Siegel, D. A. & Weber, T. 2019. Multi-faceted particle pumps drive  
808 carbon sequestration in the ocean. *Nature*, 568, 327-335.
- 809 Brownlee, E. F., Olson, R. J. & Sosik, H. M. 2016. Microzooplankton community structure investigated  
810 with imaging flow cytometry and automated live-cell staining. *Marine Ecology Progress Series*,  
811 550, 65-81.
- 812 Buck, K. R. & Newton, J. 1995. FECAL PELLET FLUX IN DABOB BAY DURING A DIATOM  
813 BLOOM - CONTRIBUTION OF MICROZOOPLANKTON. *Limnology and Oceanography*, 40,  
814 306-315.
- 815 Carpenter, E. J., Montoya, J. P., Burns, J., Mulholland, M. R., Subramaniam, A. & Capone, D. G. 1999.  
816 Extensive bloom of a N-2-fixing diatom/cyanobacterial association in the tropical Atlantic Ocean.  
817 *Marine Ecology Progress Series*, 185, 273-283.
- 818 Cassar, N., Barnett, B. A., Bender, M. L., Kaiser, J., Hamme, R. C. & Tilbrook, B. 2009. Continuous  
819 High-Frequency Dissolved O-2/Ar Measurements by Equilibrator Inlet Mass Spectrometry.  
820 *Analytical Chemistry*, 81, 1855-1864.
- 821 Chen, B. Z. 2015. Assessing the accuracy of the "two-point" dilution technique. *Limnology and*  
822 *Oceanography-Methods*, 13, 521-526.
- 823 Chen, Z. M., Kwon, Y. O., Chen, K., Fratantoni, P., Gawarkiewicz, G. & Joyce, T. M. 2020. Long-Term  
824 SST Variability on the Northwest Atlantic Continental Shelf and Slope. *Geophysical Research*  
825 *Letters*, 47.



- 826 Coplen, T. B. 1995. Reporting of stable hydrogen, carbon, and oxygen isotopic abundances - (Technical  
827 report). *Geothermics*, 24, 708-712.
- 828 de Boyer Montegut, C., Madec, G., Fischer, A. S., Lazar, A. & Iudicone, D. 2004. Mixed layer depth over  
829 the global ocean: An examination of profile data and a profile-based climatology. *Journal of*  
830 *Geophysical Research-Oceans*, 109.
- 831 Dore, J. E., Letelier, R. M., Church, M. J., Lukas, R. & Karl, D. M. 2008. Summer phytoplankton blooms  
832 in the oligotrophic North Pacific Subtropical Gyre: Historical perspective and recent  
833 observations. *Progress in Oceanography*, 76, 2-38.
- 834 Dugdale, R. C. & Goering, J. J. 1967. Uptake of new and regenerated forms of nitrogen in primary  
835 productivity. *Limnology and Oceanography*, 12, 196-206.
- 836 Emerson, S. 2014. Annual net community production and the biological carbon flux in the ocean. *Global*  
837 *Biogeochemical Cycles*, 28, 14-28.
- 838 Field, C. B., Behrenfeld, M. J., Randerson, J. T. & Falkowski, P. 1998. Primary production of the  
839 biosphere: Integrating terrestrial and oceanic components. *Science*, 281, 237-240.
- 840 Finkel, Z. V., Beardall, J., Flynn, K. J., Quigg, A., Rees, T. A. V. & Raven, J. A. 2010. Phytoplankton in  
841 a changing world: cell size and elemental stoichiometry. *Journal of Plankton Research*, 32, 119-  
842 137.
- 843 Foster, R. A. & Zehr, J. P. 2006. Characterization of diatom-cyanobacteria symbioses on the basis of  
844 *nifH*, *hetR* and 16S rRNA sequences. *Environmental Microbiology*, 8, 1913-1925.
- 845 Foster, R. A. & Zehr, J. P. 2019. Diversity, Genomics, and Distribution of Phytoplankton-  
846 Cyanobacterium Single-Cell Symbiotic Associations. In: GOTTESMAN, S. (ed.) *Annual Review*  
847 *of Microbiology*, Vol 73.
- 848 Friedlingstein, P., Jones, M. W., O'Sullivan, M., Andrew, R. M., Bakker, D. C. E., Hauck, J., Le Quere,  
849 C., Peters, G. P., Peters, W., Pongratz, J., Sitch, S., Canadell, J. G., Ciais, P., Jackson, R. B., Alin,  
850 S. R., Anthoni, P., Bates, N. R., Becker, M., Bellouin, N., Bopp, L., Chau, T. T. T., Chevallier, F.,  
851 Chini, L. P., Cronin, M., Currie, K. I., Decharme, B., Djeutchouang, L. M., Dou, X. Y., Evans,  
852 W., Feely, R. A., Feng, L., Gasser, T., Gilfillan, D., Gkritzalis, T., Grassi, G., Gregor, L., Gruber,  
853 N., Gurses, O., Harris, I., Houghton, R. A., Hurtt, G. C., Iida, Y., Ilyina, T., Luijckx, I. T., Jain, A.,  
854 Jones, S. D., Kato, E., Kennedy, D., Goldewijk, K. K., Knauer, J., Korsbakken, J. I., Kortzinger,  
855 A., Landschutzer, P., Lauvset, S. K., Lefevre, N., Lienert, S., Liu, J. J., Marland, G., McGuire, P.  
856 C., Melton, J. R., Munro, D. R., Nabel, J., Nakaoka, S. I., Niwa, Y., Ono, T., Pierrot, D., Poulter,  
857 B., Rehder, G., Resplandy, L., Robertson, E., Rodenbeck, C., Rosan, T. M., Schwinger, J.,  
858 Schwingshackl, C., Seferian, R., Sutton, A. J., Sweeney, C., Tanhua, T., Tans, P. P., Tian, H. Q.,  
859 Tilbrook, B., Tubiello, F., van der Werf, G. R., Vuichard, N., Wada, C., Wanninkhof, R., Watson,  
860 A. J., Willis, D., Wiltshire, A. J., Yuan, W. P., Yue, C., Yue, X., Zaehle, S. & Zeng, J. Y. 2022.  
861 Global Carbon Budget 2021. *Earth System Science Data*, 14, 1917-2005.
- 862 Garcia, H. E. & Gordon, L. I. 1992. Oxygen solubility in water: better fitting equations. *Limnology and*  
863 *Oceanography*, 37, 1307-1312.
- 864 Gaysina, L. A., Saraf, A. & Singh, P. 2019. Chapter 1 - Cyanobacteria in Diverse Habitats. In: MISHRA,  
865 A. K., TIWARI, D. N. & RAI, A. N. (eds.) *Cyanobacteria*. Academic Press.
- 866 Grosse, J., Bombar, D., Hai, N. D., Lam, N. N. & Voss, M. 2010. The Mekong River plume fuels  
867 nitrogen fixation and determines phytoplankton species distribution in the South China Sea  
868 during low- and high-discharge season. *Limnology and Oceanography*, 55, 1668-1680.
- 869 Hama, T., Miyazaki, T., Ogawa, Y., Iwakuma, T., Takahashi, M., Otsuki, A. & Ichimura, S. 1983.  
870 Measurement of photosynthetic production of a marine phytoplankton population using a stable  
871 <sup>13</sup>C isotope. *Marine Biology*, 73, 31-36.
- 872 Hamme, R. C. & Emerson, S. 2004. The solubility of neon, nitrogen and argon in distilled water and  
873 seawater. *Deep Sea Research I*, 51, 1517-1528.
- 874 Hendricks, M. B., Bender, M. L. & Barnett, B. A. 2004. Net and gross O<sub>2</sub> production in the Southern  
875 Ocean from measurements of biological O<sub>2</sub> saturation and its triple isotope composition. *Deep-*  
876 *Sea Research Part I-Oceanographic Research Papers*, 51, 1541-1561.



- 877 Jin, X., Gruber, N., Dunne, J. P., Sarmiento, J. L. & Armstrong, R. A. 2006. Diagnosing the contribution  
878 of phytoplankton functional groups to the production and export of particulate organic carbon,  
879 CaCO<sub>3</sub>, and opal from global nutrient and alkalinity distributions. *Global Biogeochemical*  
880 *Cycles*, 20.
- 881 Juranek, L. W., Hamme, R. C., Kaiser, J., Wanninkhof, R. & Quay, P. D. 2010. Evidence of O<sub>2</sub>  
882 consumption in underway seawater lines: Implications for air-sea O<sub>2</sub> and CO<sub>2</sub> fluxes.  
883 *Geophysical Research Letters*, 37, doi:10.1029/2009GL040423.
- 884 Juranek, L. W. & Quay, P. D. 2005. In vitro and in situ gross primary and net community production in  
885 the North Pacific Subtropical Gyre using labeled and natural abundance isotopes of dissolved O<sub>2</sub>.  
886 *Global Biogeochemical Cycles*, 19, doi:10.1029/2004GB002384.
- 887 Juranek, L. W. & Quay, P. D. 2013. Using Triple Isotopes of Dissolved Oxygen to Evaluate Global  
888 Marine Productivity. In: CARLSON, C. A. & GIOVANNONI, S. J. (eds.) *Annual Review of*  
889 *Marine Science*, Vol 5. Palo Alto: Annual Reviews.
- 890 Kalnay, E., Kanamitsu, M., Kistler, R., Collins, W., Deaven, D., Gandin, L., Iredell, M., Saha, S., White,  
891 G., Woollen, J., Zhu, Y., Chelliah, M., Ebisuzaki, W., Higgins, W., Janowiak, J., Mo, K. C.,  
892 Ropelewski, C., Wang, J., Leetmaa, A., Reynolds, R., Jenne, R. & Joseph, D. 1996. The  
893 NCEP/NCAR 40-year reanalysis project. *Bulletin of the American Meteorological Society*, 77,  
894 437-471.
- 895 Kara, A. B., Rochford, P. A. & Hurlburt, H. E. 2000. An optimal definition for ocean mixed layer depth.  
896 *Journal of Geophysical Research-Oceans*, 105, 16803-16821.
- 897 Karl, D. M., Church, M. J., Dore, J. E., Letelier, R. M. & Mahaffey, C. 2012. Predictable and efficient  
898 carbon sequestration in the North Pacific Ocean supported by symbiotic nitrogen fixation.  
899 *Proceedings of the National Academy of Sciences of the United States of America*, 109, 1842-  
900 1849.
- 901 Karmalkar, A. V. & Horton, R. M. 2021. Drivers of exceptional coastal warming in the northeastern  
902 United States. *Nature Climate Change*, 11, 854+.
- 903 Kemp, A. E. S. & Villareal, T. A. 2013. High diatom production and export in stratified waters - A  
904 potential negative feedback to global warming. *Progress in Oceanography*, 119, 4-23.
- 905 Kemp, A. E. S. & Villareal, T. A. 2018. The case of the diatoms and the muddled mandalas: Time to  
906 recognize diatom adaptations to stratified waters. *Progress in Oceanography*, 167, 138-149.
- 907 Kistler, R., Kalnay, E., Collins, W., Saha, S., White, G., Woollen, J., Chelliah, M., Ebisuzaki, W.,  
908 Kanamitsu, M., Kousky, V., van den Dool, H., Jenne, R. & Fiorino, M. 2001. The NCEP-NCAR  
909 50-year reanalysis: Monthly means CD-ROM and documentation. *Bulletin of the American*  
910 *Meteorological Society*, 82, 247-267.
- 911 Landry, M. R., Brown, S. L., Rii, Y. M., Selph, K. E., Bidigare, R. R., Yang, E. J. & Simmons, M. P.  
912 2008. Depth-stratified phytoplankton dynamics in Cyclone Opal, a subtropical mesoscale eddy.  
913 *Deep-Sea Research Part II-Topical Studies in Oceanography*, 55, 1348-1359.
- 914 Landry, M. R. & Calbet, A. 2004. Microzooplankton production in the oceans. *Ices Journal of Marine*  
915 *Science*, 61, 501-507.
- 916 Lange, M. & van Sebille, E. 2017. Parcels v0.9: prototyping a Lagrangian ocean analysis framework for  
917 the petascale age. *Geosci. Model Dev.*, 10, 4175-4186.
- 918 Li, G. C., Cheng, L. J., Zhu, J., Trenberth, K. E., Mann, M. E. & Abraham, J. P. 2020. Increasing ocean  
919 stratification over the past half-century. *Nature Climate Change*, 10, 1116-U76.
- 920 Li, Y., Fratantoni, P. S., Chen, C. S., Hare, J. A., Sun, Y. F., Beardsley, R. C. & Ji, R. B. 2015. Spatio-  
921 temporal patterns of stratification on the Northwest Atlantic shelf. *Progress in Oceanography*,  
922 134, 123-137.
- 923 Lindegren, M., Checkley, D. M., Ohman, M. D., Koslow, J. A. & Goericke, R. 2016. Resilience and  
924 stability of a pelagic marine ecosystem. *Proceedings of the Royal Society B-Biological Sciences*,  
925 283.



- 926 Lomas, M. W., Moran, S. B., Casey, J. R., Bell, D. W., Tiahlo, M., Whitefield, J., Kelly, R. P., Mathis, J.  
927 T. & Cokelet, E. D. 2012. Spatial and seasonal variability of primary production on the Eastern  
928 Bering Sea shelf. *Deep-Sea Research Part II-Topical Studies in Oceanography*, 65-70, 126-140.
- 929 Malviya, S., Scalco, E., Audic, S., Vincenta, F., Veluchamy, A., Poulain, J., Wincker, P., Iudicone, D., de  
930 Vargas, C., Bittner, L., Zingone, A. & Bowler, C. 2016. Insights into global diatom distribution  
931 and diversity in the world's ocean. *Proceedings of the National Academy of Sciences of the*  
932 *United States of America*, 113, E1516-E1525.
- 933 Manning, C., Stanley, R. H. R. & Lott III, D. E. 2016. Continuous Measurements of Dissolved Ne, Ar,  
934 Kr, and Xe Ratios with a Field-deployable Gas Equilibration Mass Spectrometer. *Analytical*  
935 *Chemistry*, 88, 3040-3048.
- 936 Manning, C. C., Howard, E. M., Nicholson, D. P., Ji, B. Y., Sandwith, Z. O. & Stanley, R. H. R. 2017a.  
937 Revising estimates of aquatic gross oxygen production by the triple oxygen isotope method to  
938 incorporate the local isotopic composition of water. *Geophysical Research Letters*, 44.
- 939 Manning, C. C., Stanley, R. H. R., Nicholson, D. P., Smith, J. M., Pennington, J. T., Fewings, M. R.,  
940 Squibb, M. E. & Chavez, F. P. 2017b. Impact of recently upwelled water on productivity  
941 investigated using in situ and incubation-based methods in Monterey Bay. *Journal of*  
942 *Geophysical Research-Oceans*, 122, 1901-1926.
- 943 Marrec, P., McNair, H., Franze, G., Morison, F., Strock, J. P. & Menden-Deuer, S. 2021. Seasonal  
944 variability in planktonic food web structure and function of the Northeast US Shelf. *Limnology*  
945 *and Oceanography*, 66, 1440-1458.
- 946 Mehta, A. 2022. *Spatial and Temporal Heterogeneity in Net Community Production in the Crossshelf*  
947 *Direction of the Atlantic Northeastern Shelf*. B.A. undergraduate thesis, Wellesley College.
- 948 Menden-Deuer, S. & Lessard, E. 2000. Menden-Deuer S, Lessard EJ.. Carbon to volume relationships for  
949 dinoflagellates, diatoms, and other protist plankton. *Limnol Oceanogr* 45: 569-579. *Limnology*  
950 *and oceanography*, 45, 569-579.
- 951 Micheli, F., Cottingham, K. L., Bascompte, J., Bjornstad, O. N., Eckert, G. L., Fischer, J. M., Keitt, T. H.,  
952 Kendall, B. E., Klug, J. L. & Rusak, J. A. 1999. The dual nature of community variability. *Oikos*,  
953 85, 161-169.
- 954 Millero, F. J. & Poisson, A. 1981. International One-Atmosphere Equation of State of Seawater. *Deep-*  
955 *Sea Research Part a-Oceanographic Research Papers*, 28, 625-629.
- 956 Moberg, E. A. & Sosik, H. M. 2012. Distance maps to estimate cell volume from two-dimensional  
957 plankton images. *Limnology and Oceanography-Methods*, 10, 278-288.
- 958 Morison, F., Franzè, G., Harvey, E. & Menden-Deuer, S. 2020. Light fluctuations are key in modulating  
959 plankton trophic dynamics and their impact on primary production. *Limnology and*  
960 *Oceanography Letters*, 5, 346-353.
- 961 Mouw, C. B. & Yoder, J. A. 2005. Primary production calculations in the Mid-Atlantic Bight, including  
962 effects of phytoplankton community size structure. *Limnology and Oceanography*, 50, 1232-  
963 1243.
- 964 O'Reilly, J. E. & Zetlin, C. 1998. Seasonal, horizontal and vertical distribution of phytoplankton  
965 chlorophyll a in the Northeast U.S. Continental Shelf Ecosystem. *NOAA Tech. Rep.*, .
- 966 Oliver, H., Zhang, W. F., Smith, W. O., Alatalo, P., Chappell, P. D., Hirzel, A. J., Selden, C. R., Sosik, H.  
967 M., Stanley, R. H. R., Zhu, Y. F. & McGillicuddy, D. J. 2021. Diatom Hotspots Driven by  
968 Western Boundary Current Instability. *Geophysical Research Letters*, 48.
- 969 Oliver, H., Zhang, W. G., Archibald, K. M., Hirzel, A. J., Smith, W. O., Sosik, H. M., Stanley, R. H. R. &  
970 McGillicuddy, D. J. 2022. Ephemeral Surface Chlorophyll Enhancement at the New England  
971 Shelf Break Driven by Ekman Restratification. *Journal of Geophysical Research-Oceans*, 127.
- 972 Olson, R. J. & Sosik, H. M. 2007. A submersible imaging-in-flow instrument to analyze nano-and  
973 microplankton: Imaging FlowCytobot. *Limnology and Oceanography-Methods*, 5, 195-203.
- 974 Palevsky, H. I., Quay, P. D., Lockwood, D. E. & Nicholson, D. P. 2016. The annual cycle of gross  
975 primary production, net community production, and export efficiency across the North Pacific  
976 Ocean. *Global Biogeochem. Cycles*, 30, 361-380.



- 977 Parsons, T. R., Maita, Y. & Lalli, C. M. 1984. *A Manual of Chemical & Biological Methods for Seawater*  
978 *Analysis*, Pergamon.
- 979 Prokopenko, M. G., Pauluis, O. M., Granger, J. & Yeung, L. Y. 2011. Exact evaluation of gross  
980 photosynthetic production from the oxygen triple-isotope composition of O(2): Implications for  
981 the net-to-gross primary production ratios. *Geophysical Research Letters*, 38.
- 982 Puigcorbe, V., Benitez-Nelson, C. R., Masque, P., Verdeny, E., White, A. E., Popp, B. N., Prahl, F. G. &  
983 Lam, P. J. 2015. Small phytoplankton drive high summertime carbon and nutrient export in the  
984 Gulf of California and Eastern Tropical North Pacific. *Global Biogeochemical Cycles*, 29, 1309-  
985 1332.
- 986 Pyle, A. E., Johnson, A. M. & Villareal, T. A. 2020. Isolation, growth, and nitrogen fixation rates of the  
987 *Hemiaulus-Richelia* (diatom-cyanobacterium) symbiosis in culture. *PeerJ*, 8.
- 988 Reuer, M. K., Barnett, B. A., Bender, M. L., Falkowski, P. G. & Hendricks, M. B. 2007. New estimates  
989 of Southern Ocean biological production rates from O-2/Ar ratios and the triple isotope  
990 composition of O-2. *Deep-Sea Research Part I-Oceanographic Research Papers*, 54, 951-974.
- 991 Robinson, C. & Williams, P. J. I. B. 2005. 147Respiration and its measurement in surface marine waters.  
992 *Respiration in Aquatic Ecosystems*. Oxford University Press.
- 993 Russakovsky, O., Deng, J., Su, H., Krause, J., Satheesh, S., Ma, S., Huang, Z. H., Karpathy, A., Khosla,  
994 A., Bernstein, M., Berg, A. C. & Fei-Fei, L. 2015. ImageNet Large Scale Visual Recognition  
995 Challenge. *International Journal of Computer Vision*, 115, 211-252.
- 996 Schmoker, C., Hernandez-Leon, S. & Calbet, A. 2013. Microzooplankton grazing in the oceans: impacts,  
997 data variability, knowledge gaps and future directions. *Journal of Plankton Research*, 35, 691-  
998 706.
- 999 Shearman, R. K. & Lentz, S. J. 2010. Long-Term Sea Surface Temperature Variability along the US East  
1000 Coast. *Journal of Physical Oceanography*, 40, 1004-1017.
- 1001 Shoemaker, L. G., Hallett, L. M., Zhao, L., Reuman, D. C., Wang, S. P., Cottingham, K. L., Hobbs, R. J.,  
1002 Castorani, M. C. N., Downing, A. L., Dudley, J. C., Fey, S. B., Gherardi, L. A., Lany, N.,  
1003 Portales-Reyes, C., Rypel, A. L., Sheppard, L. W., Walter, J. A. & Suding, K. N. 2022. The long  
1004 and the short of it: Mechanisms of synchronous and compensatory dynamics across temporal  
1005 scales. *Ecology*, 103.
- 1006 Spitzer, S. 2015. An Analysis of Diatom Growth Rate and the Implications for the Biodiesel Industry.  
1007 *Occum's Razor*, 5.
- 1008 Stanley, R. H. R., Jenkins, W. J., Doney, S. C. & Lott III, D. E. 2009. Noble Gas Constraints on Air-Sea  
1009 Gas Exchange and Bubble Fluxes. *Journal of Geophysical Research - Oceans*, 114,  
1010 doi:10.1029/2009JC005396.
- 1011 Stanley, R. H. R., Kirkpatrick, J. B., Barnett, B., Cassar, N. & Bender, M. L. 2010. Net community  
1012 production and gross production rates in the Western Equatorial Pacific. *Global Biogeochemical*  
1013 *Cycles*, 24, GB4001, doi:10.1029/2009GB003651.
- 1014 Stanley, R. H. R., Sandwith, Z. O. & Williams, W. J. 2015. Rates of summertime biological productivity  
1015 in the Beaufort Gyre: A comparison between the low and record-low ice conditions of August  
1016 2011 and 2012. *Journal of Marine Systems*, 147, 29-44.
- 1017 Subramaniam, A., Yager, P. L., Carpenter, E. J., Mahaffey, C., Bjorkman, K., Cooley, S., Kustka, A. B.,  
1018 Montoya, J. P., Sanudo-Wilhelmy, S. A., Shipe, R. & Capone, D. G. 2008. Amazon River  
1019 enhances diazotrophy and carbon sequestration in the tropical North Atlantic Ocean. *Proceedings*  
1020 *of the National Academy of Sciences of the United States of America*, 105, 10460-10465.
- 1021 Szegedy, C., Vanhoucke, V., Ioffe, S., Shlens, J. & Wojna, Z. Rethinking the Inception Architecture for  
1022 Computer Vision. 2016 IEEE Conference on Computer Vision and Pattern Recognition (CVPR),  
1023 27-30 June 2016 2016. 2818-2826.
- 1024 Tang, W. Y., Cerdan-Garcia, E., Berthelot, H., Polyviou, D., Wang, S. V., Baylay, A., Whitby, H.,  
1025 Planquette, H., Mowlem, M., Robidart, J. & Cassar, N. 2020. New insights into the distributions  
1026 of nitrogen fixation and diazotrophs revealed by high-resolution sensing and sampling methods.  
1027 *Isme Journal*, 14, 2514-2526.





- 1028 Teeter, L., Hamme, R. C., Ianson, D. & Bianucci, L. 2018. Accurate estimation of net community  
1029 production from O<sub>2</sub>/Ar measurements. *Global Biogeochem. Cycles*, 32.
- 1030 Townsend, D. W., Thomas, A. C., Mayer, L. M., Thomas, A. J. & Quinlan, J. A. 2006. Oceanography of  
1031 the Northwest Atlantic continental shelf. In: ROBINSON, A. R. & BRINK, K. H. (eds.) *The*  
1032 *Sea*. Harvard University Press.
- 1033 Twining, B. S., Nodder, S. D., King, A. L., Hutchins, D. A., LeClerc, G. R., DeBruyn, J. M., Maas, E. W.,  
1034 Vogt, S., Wilhelm, S. W. & Boyd, P. W. 2014. Differential remineralization of major and trace  
1035 elements in sinking diatoms. *Limnology and Oceanography*, 59, 689-704.
- 1036 Villareal, T. A., Adornato, L., Wilson, C. & Schoenbaechler, C. A. 2011. Summer blooms of diatom-  
1037 diazotroph assemblages and surface chlorophyll in the North Pacific gyre: A disconnect. *Journal*  
1038 *of Geophysical Research-Oceans*, 116.
- 1039 Wang, S., Tang, W. Y., Delage, E., Gifford, S., Whitby, H., Gonzalez, A. G., Eveillard, D., Planquette, H.  
1040 & Cassar, N. 2021. Investigating the microbial ecology of coastal hotspots of marine nitrogen  
1041 fixation in the western North Atlantic. *Scientific Reports*, 11.
- 1042 Yoder, J. A., Schollaert, S. E. & O'Reilly, J. E. 2002. Climatological phytoplankton chlorophyll and sea  
1043 surface temperature patterns in continental shelf and slope waters off the northeast US coast.  
1044 *Limnology and Oceanography*, 47, 672-682.
- 1045 Zhang, W. F., Alatalo, P., Crockford, T., Hirzel, A. J., Meyer, M. G., Oliver, H., Peacock, E., Petitpas, C.  
1046 M., Sandwith, Z., Smith, W. O., Sosik, H. M., Stanley, R. H. R., Stevens, B. L. F., Turner, J. T. &  
1047 McGillicuddy, D. J. 2023. Cross-shelf exchange associated with a shelf-water streamer at the  
1048 Mid-Atlantic Bight shelf edge. *Progress in Oceanography*, 210.